Politecnico di Milano

Analytical correction of corner singularity for the turbulent flow over riblets

Supervisor

Maurizio Quadrio

Co-Supervisor

Davide Gatti

Candidate

Andrea Rossi – 920022

Sommario

E' qui presentato un metodo di correzione dello spigolo che permette al solutore DNS delle equazioni incomprimibili di Navier-Stokes, di mantenere un'elevata efficienza computazionale anche in presenza di singolarità geometriche; tale metodo è poi applicato alle V-riblets ($\alpha = 60°$) per il calcolo delle altezze di protrusione in corrente semplice di Stokes, e in corrente turbolenta per misurare la riduzione di attrito.

Il lavoro di Luchini [15] per correggere la soluzione nell'intorno dello spigolo del problema di cavità, viene analiticamente dimostrato nel caso di una V-riblet. Una volta risolto il sistema di Stokes per la funzione di corrente ψ e la vorticità ω nel sistema di coordinate polari centrato nello spigolo, è possibile calcolare le componenti di velocità spanwise v^{st} e wall-normal w^{st} soluzioni di Stokes. Successivamente, si sostituiscono nell'equazione del momento della quantità di moto, la cui integrazione conduce all'espressione della pressione p^{st}. La componente di velocità parallela allo spigolo u^{st} è invece il risultato dell'equazione di Laplace per il problema descritto.

Il metodo viene quindi implementato nel codice DNS sviluppato da Luchini, e validato in primo luogo, mediante il confronto delle altezze di protrusione con le medesime quantità analitiche riportate in Luchini *et al.* [17], per diverse risoluzioni e aspect ratio della griglia computazionale. Si osserva un miglioramento di quasi un ordine di grandezza, quantificato dal numero di punti per riblet necessari ad avere un errore comparabile sulla differenza Δh. Vengono poi simulati a $Re_\tau = 200$ in corrente turbolenta i due casi con risoluzione più bassa, 8 e 16 punti per riblet, per misurare la riduzione di attrito $\mathscr{R}$ nell'intorno dell'ottimo della curva: $s^+ = 16$. Il codice con correzione si è avvicinato ai valori interpolati di Bechert *et al.* [3] con un errore del 2% circa sulla riduzione di attrito, mentre il codice originale non è stato nemmeno in grado di misurare una riduzione di resistenza.

Per concludere si propone un'estensione del metodo a geometrie il cui piano contenente la sezione è libero di ruotare attorno all'asse normale alla parete z lungo la direzione del flusso; e testato per tre diversi andamenti sinusoidali delle stesse V-riblets.

Abstract

A corner correction method capable to keep high computational efficiency even for bodies with geometric singularities is here presented and applied to the V-shaped riblets ($\alpha = 60°$) in simple Stokes flow for the protrusion heights computation, and in turbulent flow to measure the drag reduction.

The work of Luchini [15] to correct the solution near the edge for the cavity problem, is analytically demonstrated for a V-shaped riblet. Once the Stokes equations are solved for the stream function ψ and the vorticity ω in the polar coordinate system centred in the edge, the spanwise velocity components v^{st} and wall-normal w^{st} Stokes solutions are computed. Subsequently, substituting them into the momentum equation, the pressure p^{st} is obtained by integration. The velocity component parallel to the edge u^{st}, instead is the result of the Laplace equation for the problem described.

The method is thus implemented for the *DNS* solver of the incompressible Navier-Stokes equations developed by Luchini, and firstly validated by comparing the protrusion heights evaluated at different resolutions and aspect ratios of the computational grid, with the corresponding analytical quantities reported in Luchini *et al.* [17]. An improvement of almost an order of magnitude, quantified by the number of points per riblet necessary to have a comparable error on the difference Δh is observed. The turbulent channel is performed at $Re_\tau = 200$ for the two lowest resolution cases, 8 and 16 points per riblet, to measure the drag reduction $\mathscr{R}$ around the optimum of its curve: $s^+ = 16$. The code with corner correction approached the Bechert *et al.* [3] interpolated values of drag reduction with an error of about 2%, while the original code was even unable to measure a positive drag reduction.

Finally, an extension of the method is proposed to geometries whose plane containing the section freely rotate around the wall-normal axis z along the main flow direction; and therefore it is tested for three different sinusoidal geometries of the same V-shaped riblets.

Contents

Contents

List of Figures

List of Tables

Chapter 1

Introduction

In the perspective of turbulence viewed like deterministic events in a chaotic background, it is reasonable thinking of intervening on these processes to develop techniques, devices to modify their statistics and therefore to control the flow. The idea, in fact, that near-wall coherent structures within the turbulent boundary layer could be modified to achieve drag reduction was likely influenced by pioneering works of Kline *et al.* [14] and Brown & Roshko [4]. However, they have to deal with great complexity in understanding the physics hidden behind, and the difficulties of designing a control system both reliable and convenient at the same time. Several active and passive techniques to reduce frictional drag were then introduced, although often only proof of concept based on numerical simulations or laboratory experiments are available. One of the first systems discovered very appealingly both for its realization simplicity, and above all, for its completely passive nature are the riblets.

1.1 Riblets

Riblets are small surface protrusions aligned with the direction of flow, which confer an anisotropic roughness to a surface. The observation that such corrugations occur naturally on the skin of sharks (Burdak [6]; Chernyshov & Zayets [7]) sparked the interest of fluid-dynamicists by studying their behaviour intensively (Bechert, Hoppe & Reif [2]; Sawyer & Winter [20]; Choi [8]; McLean, George-Falvy & Sullivan [18]; Bechert *et al.* [3]).

 The simple and well-controlled way to evaluate the friction drag reduction is typically characterized directly in terms of the drag reduction rate $\mathscr{R}$, namely the relative change in the friction coefficient C_f of the flow between the controlled case and the
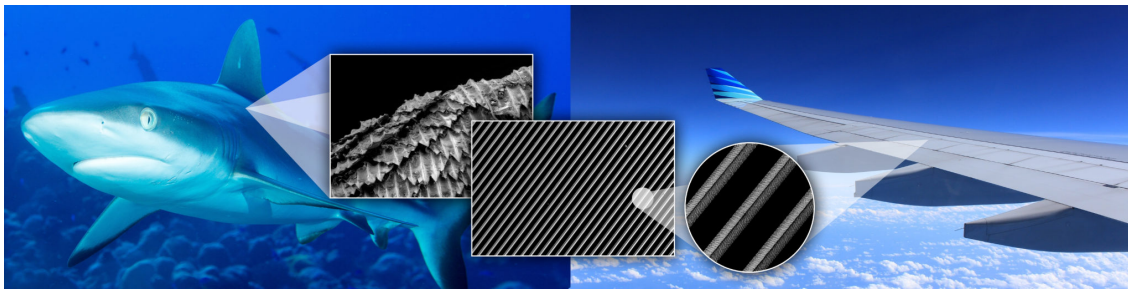
Figure 1.1. On the left riblets oriented in the streamwise direction on the mid-body region of the skin shark (length: 100–$200\mu m$). On the right the riblets applied on a wing's aircraft.

reference case:

$$\mathscr{R} = 1 - \frac{C_f}{C_{f,0}} \tag{1.1}$$

In this definition, the subscript '0' indicates a measured quantity in the reference case, and the friction coefficient is defined as

$$C_f = 2\frac{\tau_w}{\rho U_b^2} \tag{1.2}$$

where τ_w is the wall-shear stress, ρ is the fluid density and U_b is the bulk velocity. For riblets of a given aspect ratio, it is known from the most comprehensive compilations of riblet experiments (Walsh & Lindemann [23], Walsh [24], Bruse *et al.* [5] and Bechert *et al.* [3]), that the spanwise peak-to-peak spacing s of the riblet crests determines the presence and amount of drag reduction, the maximum of which is around 10%. In particular small values of s identify the so-called viscous regime: in this case, the drag reduction is proportional to the size of the riblet and the mechanism responsible for the drag reduction depends on the riblet ability to oppose the cross-flow more than the parallel one, estimable with the simple Stokes flow (Luchini *et al.* [17]; Spalart & McLean [21]). This proportionality is lost when the spacing of the riblets scaled in viscous units $s^+ = su_\tau/\nu$ (i.e. adimensionalized by the wall friction velocity of the flow and the kinematic viscosity ν of the fluid), or for better characterization, the groove cross-section A_g^+ (Garcia-Mayoral & Jiménez [10]) becomes sufficiently large. The optimum is for $A_g^{+1/2} \approx 11$. The viscous regime breaking has been studied numerically by Garcia-Mayoral & Jiménez [11], and experimentally by Gatti *et al.* [13]. It is worth noticing the superscript + indicates non-dimensionalisation in viscous units.

The application interest of this system led to testing them first on full-size aircraft in flight conditions (Walsh, Sellers & McGinley [25]), and later on flight tests of a commercial aircraft (Airbus 320) with riblets over 70% of its surface (Szodruch [22]),

estimating an overall drag reduction of 2%, indirectly assessed by the change in fuel consumption. A summary of those tests, including maintenance and durability issues, can be found in Robert [19].

More difficult, on the other hand, is the corresponding numerical verification of the riblets performance for Reynolds number values Re typical of industrial applications. In the aim of numerically testing them in the viscous drag reduction regime for increasingly higher Reynolds numbers, becomes important to be able to correctly study these systems using few points.

The geometric singularity that characterizes this technology is also directly responsible for its drag reduction capabilities, and makes numerical simulations extremely challenging.

In this report, a possible solution based on Luchini [15] is proposed. The above problem in fact can be removed if the local behaviour of the solution close to the singularity is analytically determined and compensated for. The key of doing so it is in observing that, since the velocity gradients become infinitely large at these corners, viscous effects dominate there, and the local behaviour can therefore be obtained from the Stokes equations, i.e. the Stokes-Navier equations with convective-terms neglected.

The study is therefore conducted for a viscous Reynolds number $Re_\tau = 200$ (being $Re_\tau = u_\tau \delta / \nu$, and δ the half-height channel), on V-shaped riblets with height to spacing ratio $h/s = 0.87$. The corner correction is firstly tested, computing the protrusion heights in simple Stokes flow, then in turbulent flow around the maximum of drag reduction. More precisely $s^+ = 16$, corresponding to $A_g^{+1/2} \approx 10.6$, is considered, for the two lowest resolutions: 8 and 16 points per riblet. Computational efficiency improves significantly, almost one order of magnitude of points per riblet less, based on the protrusion heights difference Δh calculated.

1.2 Outline

Details of the *DNS* code used and numerical methods are reported in § 2, together with the procedure adopted for the computational domain definition, established on Endrikat [9], for the simulation of the reference smooth half-channel. The corner correction is then presented in § 3 focusing on the analytical approach and the code implementation, validated by comparing the protrusion heights calculated in a simple Stokes flow and the corresponding analytical values Luchini [17]. In § 4, the results of the turbulent numerical simulations are presented, reporting the values on the drag

reduction $\mathscr{R}$ and roughness function ΔU^+ curves. Future developments of the corner correction method are presented in the section § 4.2. In particular, the analytical procedure for extending the correction to a three-dimensional geometry is described, showing results of three different sinusoidal riblets configurations: standard, short, and combined.

Chapter 2

Method

Figure 2.1. Computational grid on a 2D xy (wall-normal) plane.

The simulations were performed with the *DNS* solver for incompressible Navier-Stokes equations developed by Luchini, as well as the programming language, here adapted to work on BWUniCluster 2.0.

The system is directly solved in the physical domain. No-slip boundary conditions are placed on the wall and periodic boundary conditions are employed in the x and y directions. The Cartesian coordinate system is shown in Fig.2.1 for a plane channel: x, y and z indicate the streamwise, spanwise and wall-normal coordinates, and u, v, w, the respective components of the velocity vector. The flow is assumed to be periodic in the streamwise and spanwise direction. The reference length δ is equal to half of the channel height.

The computational grid is Cartesian and staggered, with uniform cells in streamwise and spanwise directions. The pressure is placed at the intersection of the grid (Δx ix, Δy iy), while the velocity components are located half a cell postponed in the related direction: $u(ix, iy)$ is placed in (Δx $(ix + 0.5)$, Δy iy), $v(ix, iy)$ in (Δx ix,

Δy $(iy + 0.5)$). In the wall-normal direction a non-uniform grid is allowed to solve the smallest scale of the wall turbulence, and the velocity $w(ix, iy, iz)$ is located in $(\Delta x\ ix,\ \Delta y\ iy,\ zd\ (2\ iz\ +\ 1))$, where zd is the array containing the staggered points in the wall normal direction.

The temporal scheme used is the third order explicit Runge-Kutta method.

The code implements a fractional step. The projection method typically operates as a two-stage fractional step scheme, a method that uses multiple calculation steps for each numerical time-step. In the first step, the momentum equation is updated without taking into account the constraint of divergence-free updated velocity field, then the new velocity field is projected onto the space of divergence-free vector fields in the second step. Since the computational grid is staggered, at each triad (ix, iy, iz), the three momentum equations are updated in three different spatial locations. In particular, each equation is centred around the relative velocity.

The pressure gradient is taken into account with the pressure gradient forcing, null in the case of constant flow rate CFR. This corrector step implements an iterative red-black algorithm solving the equation:

$$\frac{3}{2}\frac{1}{\Delta t}(\mathbf{u}^{n+1} - \tilde{\mathbf{u}}^{n+1}) + \nabla\phi = 0 \qquad (2.1)$$

where $\tilde{\mathbf{u}}^{n+1}$ represents the velocity field after the predictor step, $\mathbf{u}^{n+1}$ is the velocity field after the entire time step, and ϕ represents the pressure correction. Solving the system between the projection of the velocity field $\mathbf{u}^{n+1}$ in the divergence-free space, and the divergence of Eq.(2.1), the pressure correction term is obtained.

The immersed boundary strategy adopted in the code is innovative and therefore requires a more detailed description.

2.1   Immersed boundary

The classical idea of considering a forcing term that simulates the presence of the body has been replaced here with an implicit correction, and the forcing term has been substituted with correction coefficients that directly multiply the unknowns. Considering the equation:

$$\frac{\partial u}{\partial t} = RHS \qquad (2.2)$$

where RHS is given by the sum of the non-linear term (NL), the Laplacian term ($lapl$), and the pressure gradient.

If now the Eq.(2.2) is discretized using for simplicity the forward Euler time scheme:

$$u^{n+1} = u^n + RHS\Delta t \qquad (2.3)$$
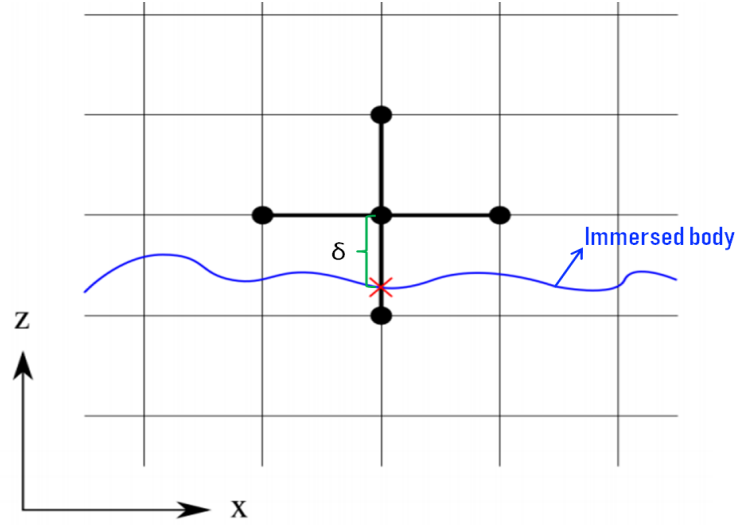
Figure 2.2. Laplacian stencil with immersed boundary correction.

with the immersed boundary correction the time advancement become:

$$u^{n+1} = \frac{u^n + RHS\Delta t}{1 + imbc\Delta t} \tag{2.4}$$

where $imbc$ is the immersed boundary coefficient. Hence, null coefficient $imbc = 0$ means no correction is made, and the time advancement works normally as there is no immersed body. On the other hand, when $imbc$ tends to infinity, the velocity tends to zero, thus reproducing the no-slip boundary condition. This wording comes from the implicit correction:

$$\begin{aligned} u^{n+1} &= u^n + RHS\Delta t - u^{n+1}imbc\Delta t \\ &= u^n + (lapl + NL + \nabla P)\Delta t - u^{n+1}imbc\Delta t. \end{aligned} \tag{2.5}$$

Assuming that very closed to the wall, where the immersed boundary correction is applied, the non-linear term and the pressure gradient are negligible, the correction only acts on the laplacian term. Further simplification of the dissertation is done by considering a uniform grid also in the z direction, with only one arm of the stencil inside the body as shown in Fig.2.2.

Focusing on the wall-normal direction of the Laplacian term:

$$lapl = \cdots + \frac{1}{\Delta z^2}(u(\cdot, iz + 1) - 2u(\cdot, iz) + u(\cdot, iz - 1)) \tag{2.6}$$

$u(\cdot, iz)$ represents the velocity $u(ix, iy, iz)$, i.e. the point where the stencil is centred. We are in fact focusing attention on the streamwise velocity, and the stencil is therefore

centred in $(\Delta x\ (ix + 0.5),\ \Delta y\ iy,\ \Delta z\ iz)$. In this way the stencil arms connect the point with the surrounding streamwise velocities. In the Eq.(2.6) only the term in the z direction has been treated explicitly, since observing Fig.2.2, it's the only part in this example that needs correction.

Please note, $u(\cdot, iz - 1)$ is null because the point is contained within the body. However, if the second-order derivative is computed with its original formula, it erroneously considers $(\cdot, iz - 1)$ as the first zero velocity point.

Therefore, calculating the second derivative using the point located on the red "X ", at distance δ from the center of the stencil, the correct laplacian would be:

$$lapl = \cdots + \frac{2u(\cdot, iz + 1)}{(\Delta z + \delta)\Delta z} - \frac{2u(\cdot, iz)}{\delta \Delta z} \tag{2.7}$$

where the u_X has already been neglected.

To have a correction that takes into account only the velocity $u(\cdot, iz)$, a non-centered scheme is adopted. The second derivative is then constructed for two successive non-centered first derivatives. Initially, the two first derivatives are expressed with backward Euler scheme, with the velocity u_X on the immersed body neglected because it is null. Finally, to obtain the second derivative at the center of the stencil, the forward Euler derivation is applied between the two points where the first derivatives were computed:

$$u''(\cdot, iz) = \frac{\frac{u(\cdot, iz+1) - u(\cdot, iz)}{\Delta z} - \frac{u(\cdot, iz) - 0}{\delta}}{\Delta z} = \frac{u(\cdot, iz + 1)}{\Delta z^2} - u(\cdot, iz)\left(\frac{1}{\Delta z^2} + \frac{1}{\delta \Delta z}\right). \tag{2.8}$$

Comparing Eq.(2.8) and Eq.(2.6)it is observed that only the middle term of the stencil needs to be corrected with the final form:

$$imbc = -\frac{1}{\Delta z^2} + \frac{1}{\delta \Delta z}. \tag{2.9}$$

The formula is here simplified for the case shown above, however the 3D nature of the immersed body stencil must be taken into account in the code.

In order to manage the totality of the geometries, at this point in time the entire domain is divided into three distinct regions: a region inside the body therefore excluded from the computation, a region that is far from the body hence without interaction, and a region that interacts with the body and thus that requires correction.

2.2 Reference smooth half-channel

The *DNS* solver was previously validated with the works of Luchini [16] and Banchetti *et al.* [1], hence it is directly presented now, the computation of the reference turbulent

	Re_τ	Re_b	L_x^+	L_y^+	U_b^+	C_f
Gatti et al.	199.7	3177	409	205	15.91	0.00790
CPG	200	3217	1500	416	16.08	0.00773

Table 2.1. The table reports Reynolds numbers Re_τ, Re_b, streamwise length in viscous units L_x^+, spanwise length in viscous units L_y^+, bulk velocity in viscous units U_b^+, friction coefficient C_f.

smooth half-channel.

The simulation is performed at constant pressure gradient CPG and $Re_\tau = 200$, whose considerations about the computational domain size are based on Endrikat [9].

In particular, in order to guarantee a correspondence between the velocity and turbulent statistics with the experimental results above the logarithmic region, i.e. the critical height z_c^+ approximately equal to 2/3 of the half-height of the channel ($\delta^+ = 1 \cdot Re_\tau$), the plane channel has a width in viscous units $L_y^+ = 416$ ($L_y = 2.08$). In fact, since the simulation is the reference case for the riblets, a suitable multiple of the riblet spacing $s^+ = 16$ that satisfies the expression $z_c^+ = 0.4 L_y^+ \approx 166.7$ is chosen. The streamwise length in viscous units $L_x^+ = 1500$ ($L_x = 7.5$), is then appropriately defined in compliance with the relation:

$$L_x^+ > \max(3L_y^+, 1000).$$

The number of mesh points in the three directions are $(nx, ny, nz) = (226, 312, 312)$. The corresponding spatial resolution in the homogeneous directions is $\Delta x^+ = 6.6$ and $\Delta y^+ = 1.3$; the wall-normal resolution increases from $\Delta z_{\min}^+ = 0.16$ near the walls to $\Delta z_{\max}^+ = 0.9$ at the centreline.

The mean streamwise velocity profile and the mean variances are shown in Fig.2.4 compared with the Gatti *et al.* [12] data for a turbulent smooth channel. Please note, the reason for the discrepancies in centreline between the results is related to the different boundary conditions: the reference smooth half-channel in fact imposes symmetric boundary conditions for the streamwise and spanwise velocity component, and an anti-symmetric boundary condition for the wall-normal velocity component at the centreline. The smooth channel instead, imposes only no-slip and no penetration boundary conditions on the walls.

The corresponding results are reported in Tab.2.1. The statistics are computed for 200 h/u_τ (h is the channel average height, i.e. δ in the present case), and for this reason the errors are here omitted because very small.
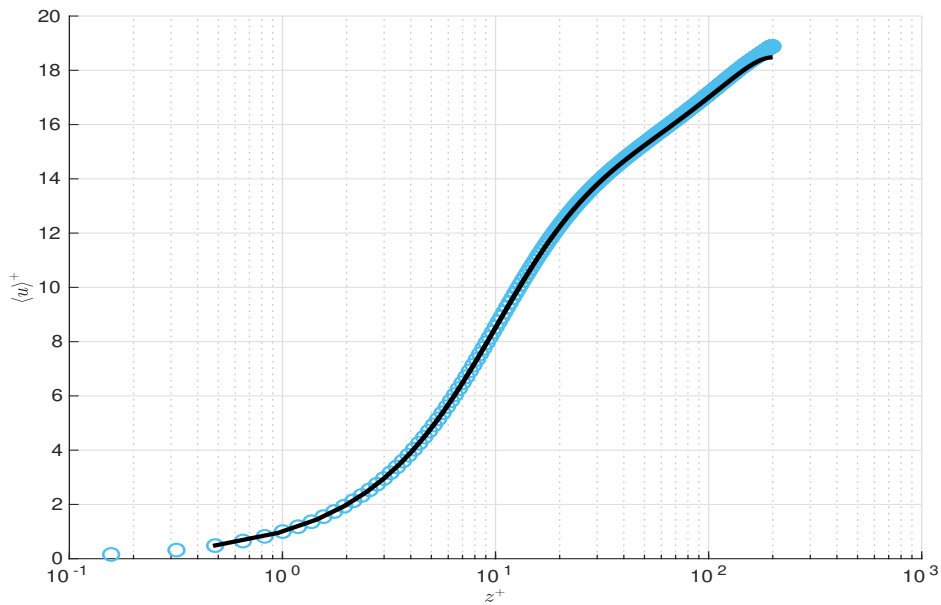
Figure 2.3. Mean streamwise velocity $\langle u \rangle^+$ as a function of the wall-normal coordinate in viscous units z^+, at $Re_\tau = 200$. ($\bigcirc$) smooth half-channel computed with Luchini *DNS* code. (——) smooth reference channel Gatti *et al.* [12]
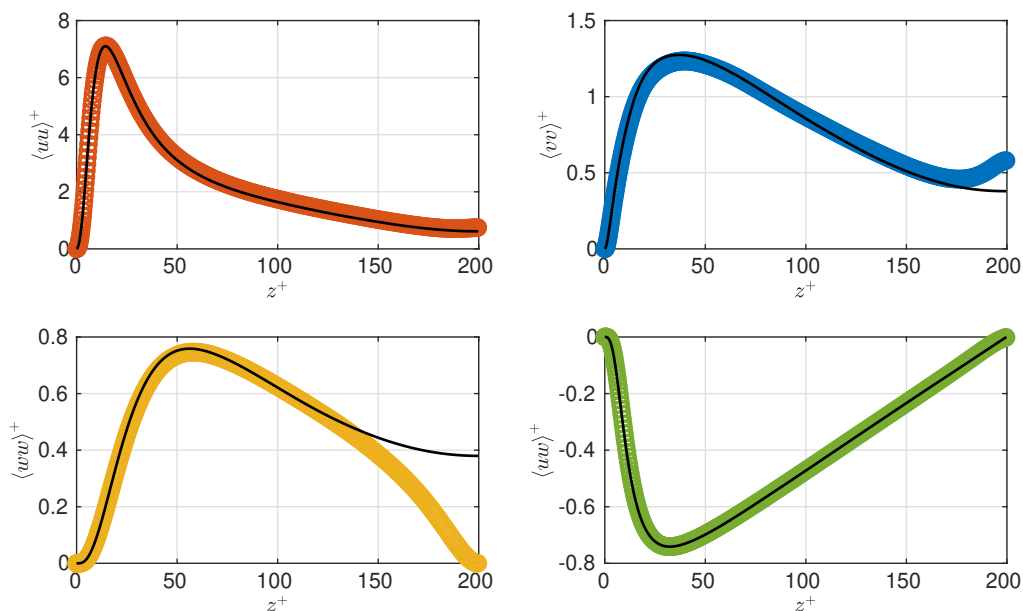
Figure 2.4. Mean variances profiles in viscous units $\langle uu \rangle^+$, $\langle vv \rangle^+$, $\langle ww \rangle^+$, $\langle uw \rangle^+$ at $Re_\tau = 200$. ($\bigcirc$) smooth half-channel computed with Luchini *DNS* code. (——) smooth channel Gatti *et al.* [12]

Chapter 3

Corner Correction

The ability of a Navier-Stokes solver to correctly measure the drag reduction for a channel with riblets, strongly depends on the reliability of the code in solving the flow around the corner. The latter is in fact responsible for the origin of numerical singularities within the solution that causes a reduction in the *DNS* code performance, making it necessary to use a large number of points around the edge, and therefore causing poor computational efficiency.

The method proposed to eliminate the problem is based on the possibility of analytically determining the solution around the singularity, and being able to compensate for it. Viscous effects dominate around the corner, and the local behaviour can be obtained from the Stokes equations, neglecting the convective terms from the complete Navier-Stokes system; which in the case of an incompressible Newtonian fluid take the (vectorized) form:

$$\begin{cases} \nabla \cdot \mathbf{u} = 0 \\ \nabla^2 \mathbf{u} - \frac{1}{\nu} \nabla p = 0. \end{cases} \tag{3.1}$$

Below is presented the analytical demonstration of the correction and its implementation for the case of V-shaped riblet. Nevertheless, the discussion is easily extendable to any 2D geometry.

3.1 Analytical correction for the corner singularity

Consider the problem represented in Fig.3.1. Near the corner, the Stokes problem (3.1) is locally reduced to solving the biharmonic equation for the stream function in the riblet tips outer space: $\Delta^2 \psi = 0$, where Δ is the Laplacian operator in two dimensions.

The equation written above can be easily figured out by resorting to the separation
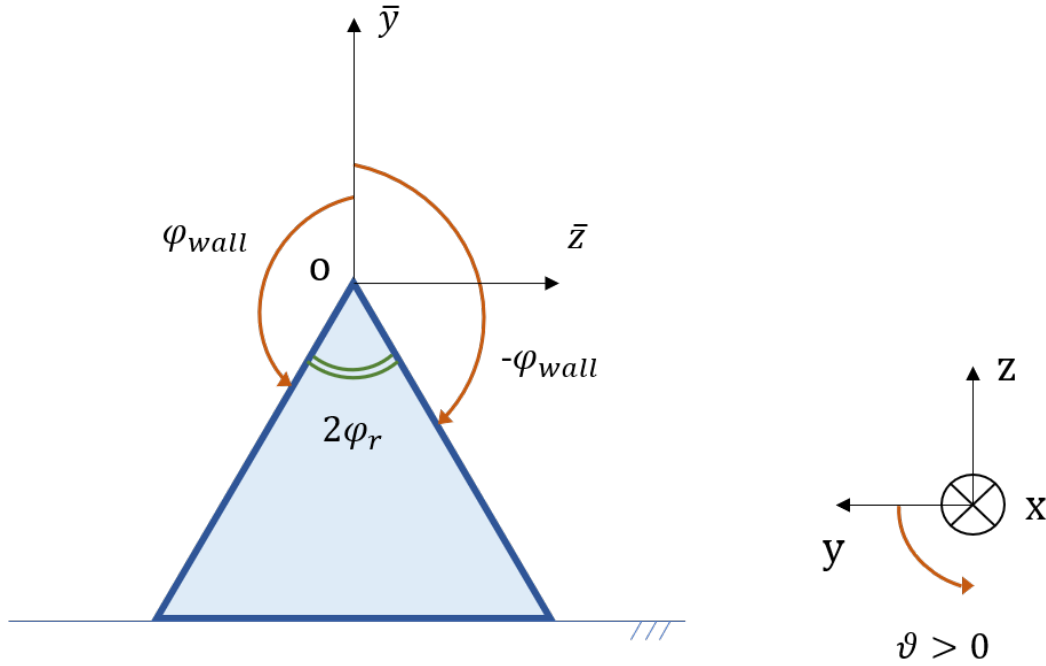
Figure 3.1. 2D V-shaped riblet section. $\bar{y} - \bar{z}$ is the local reference system centred in the riblet tip O. $\pm\varphi_{wall}$: wall location angles. $2\varphi_r$: tip riblet angle. x-y-z global reference system.

of variables in polar coordinates (r, θ). In particular, it is assumed that among the families of solutions to the $\psi - \omega$ Stokes equations exist the following form:

$$
\begin{aligned}
\psi(r, \theta) &= P(r)F(\theta) = r^{k+2}F(\theta) \\
\omega(r, \theta) &= R(r)G(\theta) = r^k G(\theta)
\end{aligned}
\tag{3.2}
$$

with $k < 0$, and having neglected the exponential with positive exponent of r, under the assumption of considering small values of r. While $F(\theta)$ and $G(\theta)$ satisfy the equations:

$$
F''(\theta) + (k + 2)^2 F(\theta) = G(\theta), \qquad G''(\theta) + k^2 G(\theta) = 0
\tag{3.3}
$$

and the general integrals are thus:

$$
\omega(r, \theta) = r^k [C_1 \cos(k\theta) + C_2 \sin(k\theta)]
$$
$$
\psi(r, \theta) = r^{k+2}\{D_1 \cos[(k+2)\theta] + D_2 \sin[(k+2)\theta] + D_3 \cos(k\theta) + D_4 \sin(k\theta)\}.
\tag{3.4}
$$

The no-slip and no penetration boundary conditions are imposed for the problem shown in Fig.3.1:

$$
\begin{cases}
v_r(r, -\varphi_{wall}) = 0 \\
v_\theta(r, -\varphi_{wall}) = 0
\end{cases}
\qquad
\begin{cases}
v_r(r, \varphi_{wall}) = 0 \\
v_\theta(r, \varphi_{wall}) = 0
\end{cases}
\tag{3.5}
$$

where $\pm\varphi_{wall}$ are the angles at which the walls are located in the specifically chosen reference system. It can be also expressed as a function of the half-angle at the riblet tips (φ_r): $\varphi_{wall} = \pi - \varphi_r$.

The expressions of v_r and v_θ instead, are obtained from the stream function partial derivatives:

$$v_r = \frac{1}{r}\frac{\partial\psi}{\partial\theta}, \qquad v_\theta = -\frac{\partial\psi}{\partial r} \tag{3.6}$$

whose expressions can be computed replacing the generic integral $\psi(r,\theta)$ (3.4):

$$\frac{\partial\psi}{\partial\theta} = r^{k+2}\big\{ - D_1(k+2)\sin\left[(k+2)\theta\right] + D_2(k+2)\cos\left[(k+2)\theta\right] - D_3 k\sin\left(k\theta\right)+$$

$$+ D_4 k\cos\left(k\theta\right)\big\}$$

$$\frac{\partial\psi}{\partial r} = (k+2)r^{k+1}\big\{D_1\cos\left[(k+2)\theta\right] + D_2\sin\left[(k+2)\theta\right] + D_3\cos\left(k\theta\right) + D_4\sin\left(k\theta\right)\big\}.$$

$$\tag{3.7}$$

Substituting the partial derivatives written above, in v_r and v_θ Eq.(3.6), and the results in the boundary conditions (3.5), the outcoming complete linear system conveniently simplified is:

$$\begin{cases} D_1(k+2)\sin\left[(k+2)\varphi_{wall}\right] + D_2(k+2)\cos\left[(k+2)\varphi_{wall}\right] + D_3 k\sin\left(k\varphi_{wall}\right)+ \\ \quad + D_4 k\cos\left(k\varphi_{wall}\right) = 0 \\ - D_1(k+2)\sin\left[(k+2)\varphi_{wall}\right] + D_2(k+2)\cos\left[(k+2)\varphi_{wall}\right] - D_3 k\sin\left(k\varphi_{wall}\right)+ \\ \quad + D_4 k\cos\left(k\varphi_{wall}\right) = 0 \\ D_1\cos\left[(k+2)\varphi_{wall}\right] - D_2\sin\left[(k+2)\varphi_{wall}\right] + D_3\cos\left(k\varphi_{wall}\right) - D_4\sin\left(k\varphi_{wall}\right) = 0 \\ D_1\cos\left[(k+2)\varphi_{wall}\right] + D_2\sin\left[(k+2)\varphi_{wall}\right] + D_3\cos\left(k\varphi_{wall}\right) + D_4\sin\left(k\varphi_{wall}\right) = 0. \end{cases}$$

Due to a suitable combination of the linear system equations, the following non-trivial solution can be extracted:

$$D_2 = D_4 = 0, \qquad \frac{D_3}{D_1} = \frac{-\cos\left[(k+2)\varphi_{wall}\right]}{\cos\left(k\varphi_{wall}\right)}. \tag{3.8}$$

It is worth noticing that the only two non-zero constants are dependent on each other, making the constant D_3 as a function of D_1.

Once a possible solution for the constants D_1, D_2, D_3, D_4 has been determined, the only remaining unknown is k. At this point, the system (3.1) is simplified by neglecting the terms pre-multiplied by the null coefficients as follows:

$$\begin{bmatrix} (k+2)\sin\left[(k+2)\varphi_{wall}\right] & k\sin\left(k\varphi_{wall}\right) \\ \cos\left[(k+2)\varphi_{wall}\right] & \cos\left(k\varphi_{wall}\right) \end{bmatrix} \begin{bmatrix} D_1 \\ D_3 \end{bmatrix} = \begin{bmatrix} 0 \\ 0 \end{bmatrix} \tag{3.9}$$

the constant k of the problem is accomplished by setting $\det(Q(k)) = 0$, where $Q(k)$ is the matrix that pre-multiplies the coefficient vector in the linear system above. The last step leading to determine k is reported:

$$\gamma \sin\left(2\varphi_{wall}\right) + \sin\left(\gamma 2\varphi_{wall}\right) = 0, \qquad \gamma = k + 1. \tag{3.10}$$

The unknown constant is thus computed by solving the Eq.(3.10) with an iterative method, e.g. the Newton method.

All the ingredients necessary to write the Stokes solution $(v_r,\ v_\theta)$ for a generic point in the section plane are revealed, and the relative expressions are the one below:

$$\begin{cases} v_r(r,\theta) = \frac{1}{r}\frac{\partial \psi}{\partial r} = r^\gamma \left\{-D_1(\gamma+1)\sin\left[(\gamma+1)\theta\right] - D_3(\gamma-1)\sin\left[(\gamma-1)\theta\right]\right\} \\ v_\theta(r,\theta) = -\frac{\partial \psi}{\partial r} = -(\gamma+1)r^\gamma \left\{D_1\cos\left[(\gamma+1)\theta\right] + D_3\cos\left[(\gamma-1)\theta\right]\right\}. \end{cases}$$
$$\tag{3.11}$$

Observing the Fig.3.2, it is possible to write the polar coordinates $(r,\ \theta)$ for a generic point A in the plane of the section:

$$r = \sqrt{(y_A - y_O)^2 + (z_A - z_O)^2}, \qquad \theta = \text{atan2}\left(\frac{y_A - y_O}{z_A - z_O}\right) \tag{3.12}$$
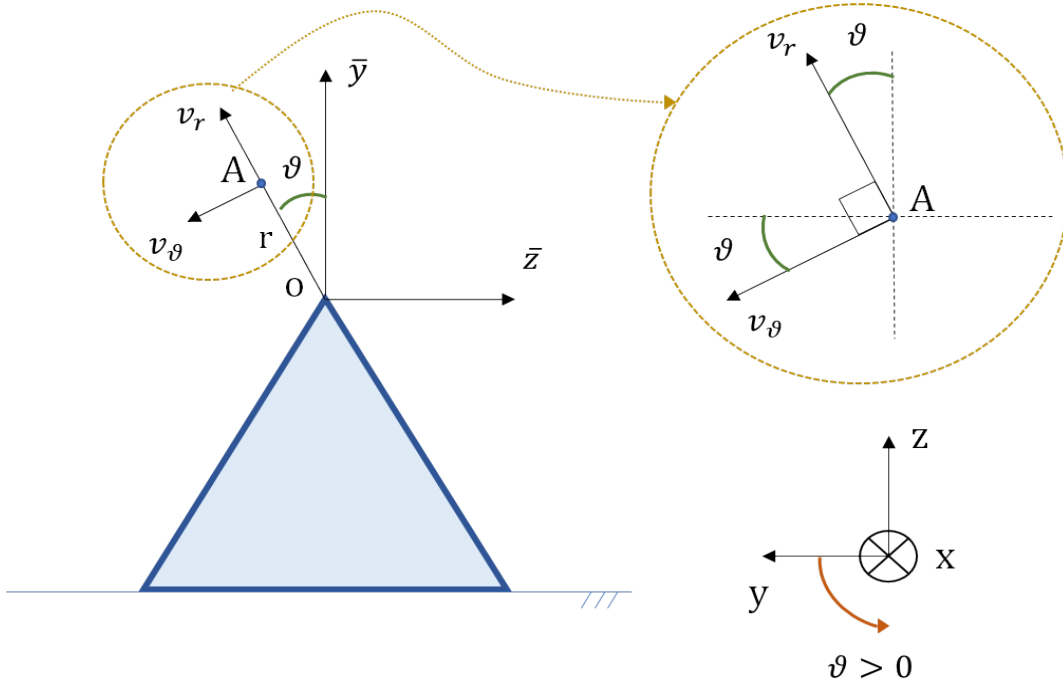
Figure 3.2. 2D V-shaped riblet section. $(r,\ \theta)$ polar coordinates of the generic point A in the local reference system $\bar{y} - \bar{z}$ centred in the riblet tip O. $(v_r,\ v_\theta)$ are the radial velocity versor and the tangential velocity versor respectively, in A.

and the relations linking the spanwise v and wall-normal w velocity components in the plane, with v_r and v_θ are then:

$$\begin{cases} v = v_r \sin(\theta) + v_\theta \cos(\theta) \\ w = v_r \cos(\theta) - v_\theta \sin(\theta). \end{cases} \tag{3.13}$$

Regarding the pressure correction term, consider the momentum equation of the Stokes problem in polar coordinates:

$$\frac{\partial p}{\partial r} = \nu \left(\frac{\partial^2 v_r}{\partial r^2} + \frac{1}{r}\frac{\partial v_r}{\partial r} + \frac{1}{r^2}\frac{\partial^2 v_r}{\partial \theta^2} - \frac{2}{r^2}\frac{\partial v_\theta}{\partial \theta} - \frac{v_r}{r^2} \right). \tag{3.14}$$

Once the v_r and v_θ partial derivatives are computed, starting from the Eq.(3.11), the *RHS* of the above equation is easily assessable and its final form is the following:

$$\frac{1}{\nu}\frac{\partial p}{\partial r} = 4D_3\gamma(1-\gamma)r^{\gamma-2}\sin[(\gamma-1)\theta]. \tag{3.15}$$

The Stokes solution for the pressure, is thus the integral of Eq.(3.15):

$$\frac{1}{\nu}p(r,\theta) = -4D_3\gamma r^{\gamma-1}\sin[(\gamma-1)\theta]. \tag{3.16}$$

In order to make the pressure continuous and symmetrical within the body, that expression is also extended within the geometry. For this reason, only for the points in the section plane where the correction is active, and which satisfy the condition $|\theta| > \varphi_{wall}$, the angle θ in the expression of the pressure (3.16) is multiplied by the following function:

$$if \ |\theta| > \varphi_{wall}: \quad \frac{1}{\nu}p(r,\theta) = -4D_3\gamma r^{\gamma-1}\sin[(\gamma-1)\theta \cdot f(\theta)]$$
$$f(\theta) = 1 + \frac{|\theta| - \pi}{\pi - \varphi_{wall}}\left(\frac{1}{\gamma-1} - 1\right). \tag{3.17}$$

The last quantity to be treated is the velocity component parallel to the edge. In this case, since the pressure is not affected by any variation, the problem is very simple and it is reduced to:

$$\nabla^2 u = 0 \ \Rightarrow \ \frac{1}{r}\frac{\partial}{\partial r}\left(r\frac{\partial u}{\partial r}\right) + \frac{1}{r^2}\frac{\partial^2 u}{\partial \theta^2} = 0. \tag{3.18}$$

The family of solutions to this equation is in the form $u(r,\theta) = R(r)F(\theta)$, which replaced in Eq.(3.18) leads to its generic expression written below:

$$u(r,\theta) = r^m[A\cos(m\theta) + B\sin(m\theta)], \qquad m > 0. \tag{3.19}$$

In this case the exponential with negative exponent is eliminated, since the correction in the direction parallel to the corner should vanish in the limit of r that goes to zero. The constant m is then computed in analogy to the problem in the plane section, by imposing again the no-slip and no penetration boundary conditions:

$$\begin{cases} u(r, \varphi_{wall}) = 0 \\ u(r, -\varphi_{wall}) = 0 \end{cases} \Rightarrow \begin{cases} r^m \left[A \cos\left(m\varphi_{wall}\right) + B \sin\left(m\varphi_{wall}\right) \right] = 0 \\ r^m \left[A \cos\left(m\varphi_{wall}\right) - B \sin\left(m\varphi_{wall}\right) \right] = 0 \end{cases} \tag{3.20}$$

in fact, adding the two equations together, m is obtained:

$$\cos\left(m\varphi_{wall}\right) = 0 \ \Rightarrow \ m = \frac{n\pi/2}{\varphi_{wall}} \qquad n = 1, 2, \dots \tag{3.21}$$

For constants A and B is concerned, when the above value of m is considered, the no-slip boundary condition requires that the constant B would be zero. The constant A, on the other hand, can take any value. Therefore, the correction for the velocity component parallel to the edge is:

$$u(r, \theta) = C r^m \cos\left(m\theta\right), \qquad m = \frac{\pi}{2\varphi_{wall}} \tag{3.22}$$

being C the generic constant, and having considered $n = 1$.

The analytical discussion is completed, and the implementation of the corner correction in the code will be now presented.

3.2 Corner correction implementation

The corner correction implementation within the *DNS* code (already described in § 2) can be divided into two main steps:

- to create the real function *edge*, able to return the coordinates of the nearest edge, given the considered point position;

- to impose in the subroutine that defines the geometry of the immersed body, the Stokes solution for the points around the edge.

3.2.1 REAL FUNCTION *edge*(REAL y_P, z_P)

The first step of the corner correction implementation process is to identify the closest edge, given the coordinates of a point P. In the case considered of V-shaped straight riblets, the problem is reduced to finding only the spanwise coordinates y_O and wall-normal z_O of the riblet vertex O, in the plane defined by the normal in the streamwise

direction $\bar{\mathbf{e}}_x = (1, 0, 0)$, positioned at the same streamwise coordinate of the point P: $x_O \equiv x_P$.

In the plane just defined, the edge coordinates are thus:

$$
\begin{cases}
(x_O = x_P) \\
y_O = [\mathsf{FLOOR}(y_P/s) + 0.5] \cdot s \\
z_O = h/2
\end{cases}
\tag{3.23}
$$

where h and s, are the height and spacing of the riblet respectively. Please note, the reference system considered has the null wall-normal coordinate at the half-height of the riblet.

3.2.2 Stokes solution

To understand how to impose the analytical Stokes solution for the three velocity components, the generic procedure adopted in the case of the streamwise velocity u will be presented.

First of all, consider the generic discrete expression of u at the temporal instant $(n+1)$, assuming for a better clearness that the temporal discretization scheme applied is the forward Euler method:

$$
\begin{aligned}
u^{n+1}(\mathbf{x}) = u^n(\mathbf{x}) + NL(u^n(\mathbf{x})) &- \frac{1}{\delta x}\left[p^n(x + \delta x/2) - p^n(x - \delta x/2)\right] + \\
+\Delta t \nu \Big[\frac{1}{\delta x^2}u^n(x + \delta x/2) &- \frac{1}{\delta x^2}u^n(x) - \frac{1}{\delta x^2}u^n(x) + \frac{1}{\delta x^2}u^n(x - \delta x/2) + \\
+\frac{1}{\delta y^2}u^n(y + \delta y/2) &- \frac{1}{\delta y^2}u^n(y) - \frac{1}{\delta y^2}u^n(y) + \frac{1}{\delta y^2}u^n(y - \delta y/2) + \\
+\frac{1}{\delta z^2}u^n(z + \delta z/2) &- \frac{1}{\delta z^2}u^n(z) - \frac{1}{\delta z^2}u^n(z) + \frac{1}{\delta z^2}u^n(z - \delta z/2) \Big].
\end{aligned}
\tag{3.24}
$$

In order to extend the expression of $u^{n+1}(\mathbf{x})$ to take into account a possible immersed body for the whole $3D$ stencil, the discrete form of the second derivative with respect to x obtained by further generalization of the coefficients modification described in § 2, Eq.(2.8) is reported:

$$
\left.\frac{\partial^2 u}{\partial x^2}\right|_i = \frac{1}{\Delta x^2}\frac{\Delta x}{d_{x_1}}u_{i+1} - \frac{1}{\Delta x^2}\frac{\Delta x}{d_{x_1}}u_i - \frac{1}{\Delta x^2}\frac{\Delta x}{d_{x_2}}u_i + \frac{1}{\Delta x^2}\frac{\Delta x}{d_{x_2}}u_{i-1}.
\tag{3.25}
$$

Subsequently the complete form of $u^{n+1}(\mathbf{x})$ is thus obtained by adding to the *RHS* of Eq.(3.24), the following terms:

$$
\cdots - \Delta t \nu \left[-\frac{1}{\delta x^2} u^{n+1}(x) - \frac{1}{\delta x^2} u^{n+1}(x) + \frac{1}{\delta x^2}\frac{\delta x}{d_{x_1}} u^{n+1}(x) + \frac{1}{\delta x^2}\frac{\delta x}{d_{x_2}} u^{n+1}(x) + \right.
$$
$$
-\frac{1}{\delta y^2} u^{n+1}(y) - \frac{1}{\delta y^2} u^{n+1}(y) + \frac{1}{\delta y^2}\frac{\delta y}{d_{y_1}} u^{n+1}(y) + \frac{1}{\delta y^2}\frac{\delta y}{d_{y_2}} u^{n+1}(y) + \quad (3.26)
$$
$$
\left. -\frac{1}{\delta z^2} u^{n+1}(z) - \frac{1}{\delta z^2} u^{n+1}(z) + \frac{1}{\delta z^2}\frac{\delta z}{d_{z_1}} u^{n+1}(z) + \frac{1}{\delta z^2}\frac{\delta z}{d_{z_2}} u^{n+1}(z) \right].
$$

The reason for blue-coloured terms is discussed later.

To introduce the corner correction inside the subroutine dedicated to modifying the coefficients that take into account the immersed body, the above terms must be integrated with the corner correction ones before adding them together to Eq.(3.24). Therefore, consider the Stokes problem in the discrete form:

$$
\frac{\partial^2 u}{\partial x_i} - \frac{1}{\nu}\frac{\partial p}{\partial x} = 0
$$
$$
\left\{ \frac{1}{\delta x^2}\frac{\delta x}{d_{x_1}} u^{st}(x + d_{x_1}) - \frac{1}{\delta x^2}\frac{\delta x}{d_{x_1}} u^{st}(x) - \frac{1}{\delta x^2}\frac{\delta x}{d_{x_2}} u^{st}(x) + \frac{1}{\delta x^2}\frac{\delta x}{d_{x_2}} u^{st}(x - d_{x_2}) + \right.
$$
$$
+ \frac{1}{\delta y^2}\frac{\delta y}{d_{y_1}} u^{st}(y + d_{y_1}) - \frac{1}{\delta y^2}\frac{\delta y}{d_{y_1}} u^{st}(y) - \frac{1}{\delta y^2}\frac{\delta y}{d_{y_2}} u^{st}(y) + \frac{1}{\delta y^2}\frac{\delta y}{d_{y_2}} u^{st}(y - d_{y_2}) +
$$
$$
\left. + \frac{1}{\delta z^2}\frac{\delta z}{d_{z_1}} u^{st}(z + d_{z_1}) - \frac{1}{\delta z^2}\frac{\delta z}{d_{z_1}} u^{st}(z) - \frac{1}{\delta z^2}\frac{\delta z}{d_{z_2}} u^{st}(z) + \frac{1}{\delta z^2}\frac{\delta z}{d_{z_2}} u^{st}(z - d_{z_2}) \right\} +
$$
$$
- \frac{1}{\nu}\left[p^{st}(x + \delta x/2) - p^{st}(x - \delta x/2) \right]\frac{1}{\delta x} = 0
$$
$$
(3.27)
$$

$(\cdot)^{st}$ represents the Stokes solution.

In analogy with the immersed boundary correction, the corner correction should be added in an implicit manner to the Eq.(3.24). For this reason, the terms with $u^{st}(x)$ in the Eq.(3.27) are splitted, and all the equation is multiplied by the ratio $u^{n+1}(x)/u^{st}(x)$:

$$
-\left[\frac{1}{\delta x^2}\frac{\delta x}{d_{x_1}} + \frac{1}{\delta x^2}\frac{\delta x}{d_{x_2}} + \frac{1}{\delta y^2}\frac{\delta y}{d_{y_1}} + \frac{1}{\delta y^2}\frac{\delta y}{d_{y_2}} + \frac{1}{\delta z^2}\frac{\delta z}{d_{z_1}} + \frac{1}{\delta z^2}\frac{\delta z}{d_{z_2}} \right] u^{st}(x) \cdot \frac{u^{n+1}(x)}{u^{st}(x)} +
$$
$$
+ \left\{ -\frac{1}{\nu}\left[p^{st}(x + \delta x/2) - p^{st}(x - \delta x/2) \right]\frac{1}{\delta x} + \frac{1}{\delta x^2}\frac{\delta x}{d_{x_1}} u^{st}(x + d_{x_1}) + \right.
$$
$$
+ \frac{1}{\delta x^2}\frac{\delta x}{d_{x_2}} u^{st}(x - d_{x_2}) + \frac{1}{\delta y^2}\frac{\delta y}{d_{y_1}} u^{st}(y + d_{y_1}) + \frac{1}{\delta y^2}\frac{\delta y}{d_{y_2}} u^{st}(y - d_{y_2}) +
$$
$$
\left. + \frac{1}{\delta z^2}\frac{\delta z}{d_{z_1}} u^{st}(z + d_{z_1}) + \frac{1}{\delta z^2}\frac{\delta z}{d_{z_2}} u^{st}(z - d_{z_2}) \right\} \cdot \frac{u^{n+1}(x)}{u^{st}(x)} = 0.
$$
$$
(3.28)
$$

Please note, the blue-coloured expression in the equation written above is equal, except for the sign, to the same blue-coloured terms added for the immersed body correction (3.26). In this way, when the correction above pre-multiplied by '$-\Delta t \nu$', is combined with the Eq.(3.26), and then added together to the *RHS* of the Eq.(3.24), the blue-coloured terms are simplified. Re-ordering the similar elements the resulting equation is:

$$
\left\{ 1 + \Delta t \nu \left[-\frac{1}{\nu} \frac{1}{u^{st}(x)} \left(p^{st}\left(x + \delta x/2\right) - p^{st}\left(x - \delta x/2\right) \right) \frac{1}{\delta x} + \frac{1}{\delta x^2} \frac{\delta x}{d_{x_1}} \frac{u^{st}(x + d_{x_1})}{u^{st}(x)} + \right.\right.
$$

$$
+ \frac{1}{\delta x^2} \frac{\delta x}{d_{x_2}} \frac{u^{st}(x - d_{x_2})}{u^{st}(x)} + \frac{1}{\delta y^2} \frac{\delta y}{d_{y_1}} \frac{u^{st}(x + d_{y_1})}{u^{st}(y)} + \frac{1}{\delta y^2} \frac{\delta y}{d_{y_2}} \frac{u^{st}(x - d_{y_2})}{u^{st}(y)} +
$$

$$
\left.\left. + \frac{1}{\delta z^2} \frac{\delta z}{d_{z_1}} \frac{u^{st}(z + d_{z_1})}{u^{st}(x)} + \frac{1}{\delta z^2} \frac{\delta z}{d_{z_2}} \frac{u^{st}(z - d_{z_2})}{u^{st}(x)} - \frac{2}{\delta x^2} - \frac{2}{\delta y^2} - \frac{2}{\delta z^2} \right] \right\} u^{n+1}(x)
$$

$$
=
$$

$$
u^n(\mathbf{x}) + NL(u^n(\mathbf{x})) - \frac{1}{\delta x} \left[p^n(x + \delta x/2) - p^n(x - \delta x/2) \right] + \Delta t \nu \left[\frac{1}{\delta x^2} u^n(x + \delta x/2) + \right.
$$

$$
- \frac{1}{\delta x^2} u^n(x) - \frac{1}{\delta x^2} u^n(x) + \frac{1}{\delta x^2} u^n(x - \delta x/2) + \frac{1}{\delta y^2} u^n(y + \delta y/2) - \frac{1}{\delta y^2} u^n(y) - \frac{1}{\delta y^2} u^n(y) +
$$

$$
\left. + \frac{1}{\delta y^2} u^n(y - \delta y/2) + \frac{1}{\delta z^2} u^n(z + \delta z/2) - \frac{1}{\delta z^2} u^n(z) - \frac{1}{\delta z^2} u^n(z) + \frac{1}{\delta z^2} u^n(z - \delta z/2) \right].
$$

$$
(3.29)
$$

Consequently, the correction coefficient that takes into account the immersed body and the corner correction for the streamwise velocity component is the red-coloured expression added to $u^{n+1}(x)$.

The procedure is repeated in the same way for the spanwise v and wall-normal w velocities. Summarizing, within the subroutine that identifies the immersed body, can be found:

1. constants definition D_1, D_3 and γ: in particular D_1 is taken equal to one for simplicity, D_3 respects the relation (3.8), γ is obtained by solving the Eq.(3.10);

2. two functions are defined *locsol*(REAL y_P, z_P) and *locpsol*(REAL y_P, z_P). The first one, once verified that the point P is not inside the immersed body, it returns, depending on the direction considered, the velocity component of the Stokes solution. The second one returns the Stokes pressure;

3. finally, if the considered point is sufficiently close to the edge:

$$
(y_P - y_O)^2 + (z_P - z_O)^2 \le (3\Delta y)^2.
$$

Stokes analytical solutions are then evaluated by calling the functions *locsol* and *locpsol*, and again depending on the direction considered, the corrective coefficient found in the Eq.(3.29) is computed.

3.3 Protrusion heights validation

A first verification and validation of the corner correction implemented is the comparison with the only quantity analytically known: the protrusion height.

The protrusion height is the distance below the riblets tip where the virtual origin of the velocity profile can be extrapolated. This quantity, if suitably dimensionless for the period of the corrugation, is a purely geometric parameter dependent only on the shape of the wall corrugations and neither on their size nor on the actual speed of the driving fluid. Based on this definition, Luchini [17] established the longitudinal protrusion height $h_\parallel$ and the transverse protrusion height $h_\perp$, representing the virtual origin of the longitudinal and transverse velocity profile respectively.

In this way, as the main flow (longitudinal or cross depending on the case considered) is concerned, the corrugated wall is equivalent to a plane wall located at a distance below the riblet tips equal to the protrusion height. When the virtual plane seen by the transverse flow lies above the longitudinal one, as shown in Fig.3.3, the level of near-wall turbulence is reduced. Considering the virtual origin in the riblet tips has

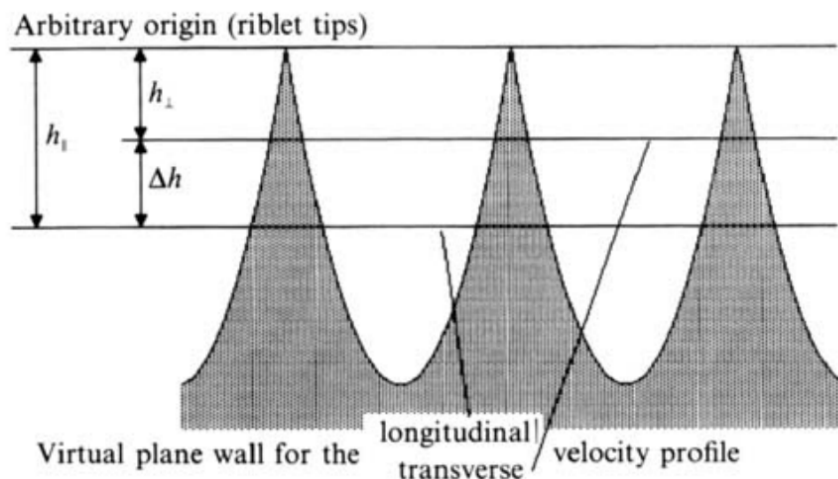Figure 3.3.   Interrelations between the protrusion heights and the positions of the virtual plane walls seen by longitudinal and transverse flow.

no particular meaning, and any physically significant parameter must be independent of the origin choice. The only combination of the two protrusion heights that has this property is their difference $\Delta h = h_\parallel - h_\perp$, i.e. the distance between the two

virtual plane walls seen by the longitudinal and cross flow. Δh provides a quantitative characterization of itself and how much the corrugated wall hinders the cross-flow more than the longitudinal flow, and it is the only parameter on which the behaviour of the turbulent boundary layer can depend. Luchini demonstrates and analytically calculates the protrusion heights values as a function of the riblet geometry considered: e.g. for the V-shaped riblet, it is a function of the height to spacing ratio h/s. He used the steady Stokes equations, and the reason lies in the inertia and convective terms of the Navier-Stokes equations which are roughly the same order of magnitude in a turbulent boundary layer, and when the latter are negligible the former are too. To compare the actual improvement of the corner correction, a single V-shaped riblet is numerically simulated, with a ratio $h/s = 0.87$, in which the non-linear terms are neglected. An initial linear streamwise (or spanwise) velocity profile is set, with a unit velocity u (or v) boundary condition in the centreline.

The virtual origin of the wall is then extrapolated from the resulting linear velocity profile and normalized for the riblet spacing to obtain the normalized longitudinal (cross) protrusion height. The computation is repeated for different values of resolution and cell aspect ratio ($\mathcal{R} = \Delta y/\Delta z$), using the code with and without correction. Tab.3.1 shows the protrusion heights resulted and their absolute relative errors for the different resolutions and codes considered.

From Fig.3.4 it is possible to observe that in the case of the code with edge correction (EC), the values of Δh oscillate close to the analytical value with different behaviours depending on the aspect ratio, while in the case of the original code (OC) Δh approaches gradually to the exact value. In particular, the difference of points such that the OC case assumes comparable error values on Δh, with the EC case is approximately one order of magnitude.

Among the several cases reported in Tab.3.1, the ones that will be analyzed in turbulent flow are highlighted in red. Precisely at $\mathcal{R} = 1$, the one with the lowest resolution (8 points per riblet, EC8 vs OC8) and the one with double resolution (16 points per riblet, EC16 vs OC16) are selected. The respective normalized protrusion heights values are compared in Fig.3.5 for the different codes used with the Luchini [17] analytical curves. Please note, the EC case studies (on the right), are able to estimate the three quantities very well, especially the high resolution one, from which reliable drag reduction measurements can be expected. The same can't be said for the original OC code (on the left), where the transverse protrusion height presents a high error for both resolutions and poor drag reduction measurements will be expected. The value of Δh for OC8, falls even outside of the figure since negative.

Type	$\mathcal{R}$	N_y	$h_\parallel$	$\frac{|h_\parallel - \bar{h}_\parallel|}{\bar{h}_\parallel}$	$h_\perp$	$\frac{|h_\perp - \bar{h}_\perp|}{\bar{h}_\perp}$	Δh	$\frac{|\Delta h - \Delta \bar{h}|}{\Delta \bar{h}}$
EC	0.5	8	0.1865	0.0873	0.09614	0.187	0.09033	0.00187
EC	1.0	8	0.1582	0.0773	0.07820	0.0345	0.08004	0.116
EC	1.5	8	0.1728	0.00758	0.09917	0.224	0.07363	0.186
EC	0.5	16	0.1667	0.0279	0.07274	0.102	0.09398	0.0385
EC	1.0	16	0.1690	0.0149	0.07868	0.0286	0.09027	0.00256
EC	1.5	16	0.1683	0.0186	0.1022	0.261	0.06615	0.269
EC	0.5	32	0.1698	0.00991	0.07805	0.0365	0.09175	0.0139
EC	1.0	32	0.1710	0.00309	0.09497	0.172	0.07598	0.160
EC	1.5	32	0.1708	0.00414	0.08838	0.0911	0.08241	0.0894
EC	0.5	64	0.1719	0.00251	0.08026	0.00916	0.09167	0.0130
EC	1.0	64	0.1714	0.000875	0.08550	0.0555	0.08585	0.0514
EC	1.5	64	0.1712	0.00198	0.08246	0.0180	0.08870	0.0199
OC	0.5	8	0.1777	0.0360	0.1395	0.722	0.03816	0.578
OC	1.0	8	0.1522	0.112	0.1560	0.926	-0.00376	1.04
OC	1.5	8	0.1596	0.0696	0.1599	0.974	-0.00035	1.00
OC	0.5	16	0.1620	0.0551	0.1368	0.689	0.02520	0.722
OC	1.0	16	0.1654	0.0357	0.1142	0.410	0.05120	0.434
OC	1.5	16	0.1649	0.0384	0.1217	0.502	0.04325	0.522
OC	0.5	32	0.1708	0.00408	0.1063	0.313	0.06446	0.288
OC	1.0	32	0.1693	0.0129	0.09817	0.212	0.07112	0.214
OC	1.5	32	0.1689	0.0153	0.1002	0.237	0.06872	0.2407
OC	0.5	64	0.1718	0.00181	0.09197	0.135	0.07984	0.118
OC	1.0	64	0.1705	0.00583	0.09045	0.117	0.08006	0.115
OC	1.5	64	0.1701	0.00805	0.08944	0.104	0.08068	0.109

Table 3.1. Normalized protrusion heights results. Type: code used, EC edge correction, OC original code. $\mathcal{R}$: aspect ratio. N_y: spanwise points per riblet. $h_\parallel$, $h_\perp$, Δh: longitudinal and cross normalized protrusion height computed, and their difference. $\frac{|(\cdot) - \bar{(\cdot)}|}{(\cdot)}$: relative error wrt Luchini [17] exact analytical value. The lines written in red are the cases simulated in turbulent flow. The values highlighted in yellow show two cases EC8 and OC64 for $\mathcal{R} = 1$ with the Δh relative error similar.
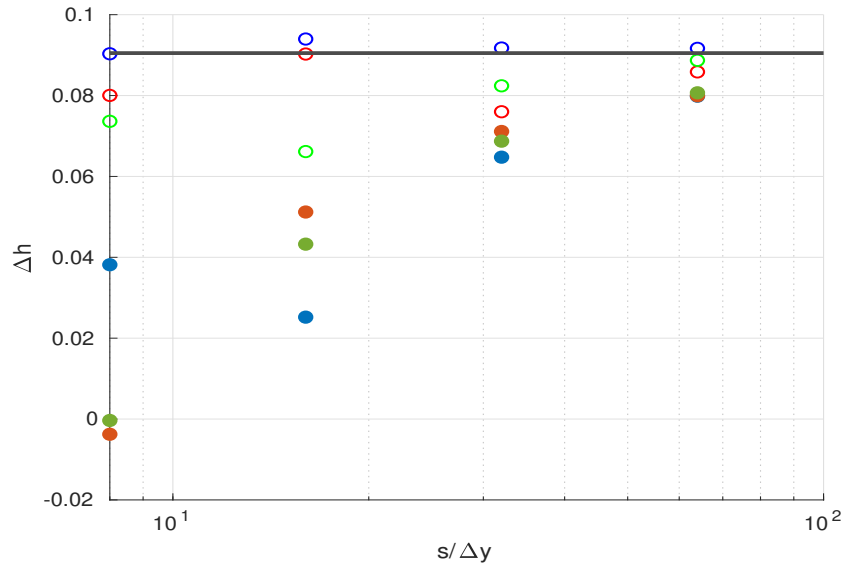
Figure 3.4. Protrusion heights difference Δh as a function of the riblet spacig to spanwise resolution ratio. (——) Luchini [17] exact analytical value. (○) edge correction (EC) case. (●) original case (OC). The three colours are related to the apect ratio of the computational cell: blue: $\mathit{AR} = 0.5$, red: $\mathit{AR} = 1.0$, green: $\mathit{AR} = 1.5$. For each case the resolutions considered are [8, 16, 32, 64] points per riblet.
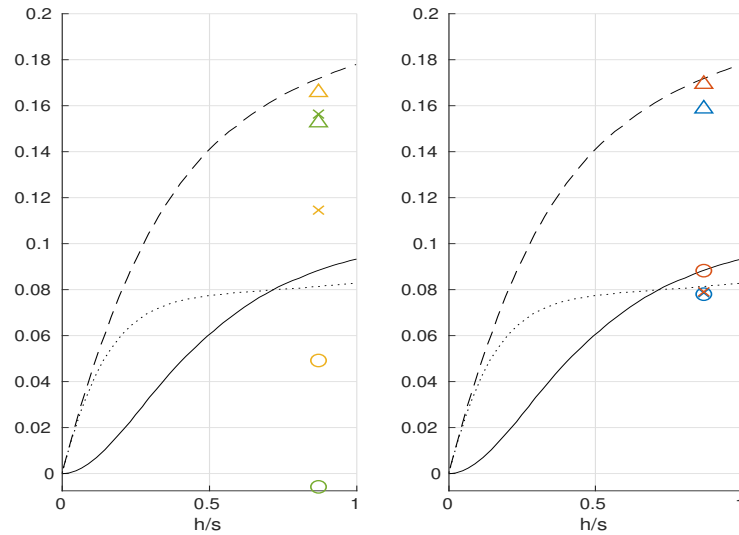
Figure 3.5. Normalized protrusion heights. On the left the original case: green OC8, yellow OC16. On the right the edge correction case: blue EC8, red EC16. Parallel (- - - -), cross (——) protrusion heights and their difference (·········), Luchini [17] reference. Parallel (△), cross (×) protrusion heights and their difference (○) computed for V-shaped riblet $h/s = 0.87$. Computational cell $\mathit{AR} = 1$.

Chapter 4

Turbulent drag reduction by riblets

The final verification in turbulent flow for the corner correction is then computed for the V-shaped riblets case shown in § 3.3, with unitary $Æ$ and for the two lowest resolution: 8 points per riblet, and 16 points per riblet.

To test the reliability of the correction in measuring the drag reduction $\mathscr{R}$ even for low resolutions, a riblet spacing in viscous units around the optimum of the drag reduction curve is considered, i.e. $s^+ = 16$.

The simulation is performed for a half-channel of height $\delta = 1 + h/2$, i.e. the average height of the channel is unitary. The viscous Reynolds number is equal to the reference smooth case $Re_\tau = 200$, and the forcing strategy chosen is CPG. The considerations about the computational domain dimensions are the same discussed in § 2.2, and the streamwise and spanwise length are identical to the smooth case. The number of points in the homogeneous directions are ($N_x = 226$, $N_y = 208$) for the low resolution case L, ($N_x = 226$, $N_y = 416$) for the higher one H. The spatial resolutions are reported in Tab.4.1 together with the simulations parameters.

Once the flow rate initial oscillation settles down, the simulations are performed for 300 h/u_τ (here h is the channel average height), which for the most expensive simulation correspond to approximately 100 hours of computation with 6×40 cores.

Case	Δx^+	Δy^+	$\Delta z^+_{\min}$	$\Delta z^+_{\max}$	L_x^+	L_y^+	h/s	s^+	$A_g^{+1/2}$
L	6.6	2.0	2.0	3.0	1500	416	0.87	16	10.6
H	6.6	1.0	1.0	3.0	1500	416	0.87	16	10.6

Table 4.1. Simulation parameters. $\Delta(\cdot)^+$ spatial resolutions. $L_{(\cdot)}^+$ domain lengths. h/s riblet height to spacing ratio. s^+ riblet spacing. $A_g^{+1/2}$ root square of the groove cross-section. $(\cdot)^+$ stands for viscous units.

4.1 Results

The turbulent results are now presented in terms of drag reduction $\mathscr{R}$ and roughness function ΔU^+: the effect of rough surfaces is also classically quantified via the downward shift ΔU^+ of the logarithmic distribution of the mean streamwise velocity profile $\langle u \rangle^+$ in the wall-normal direction z^+.

The roughness function is computed with the formula proposed by Gatti *et al.* [13]:

$$\Delta U^+ = \kappa^{-1} \log \frac{Re_\tau}{Re_{\tau_0}} - \Delta U_c^+ \tag{4.1}$$

where κ is the Von Kármán constant, the subscript 0 refers to the reference plane channel, and ΔU_c^+ is the centreline velocity defect. Since the riblets and reference simulations are performed at constant pressure gradient CPG and for the same viscous Reynolds number Re_τ, the roughness function will be given by the centreline velocity defect $\Delta U^+ = -\Delta U_c^+$.

The numerical results are reported in Tab.4.2 and compared in Fig.4.1 with the Bechert *et al.* [3] interpolated data of V-shaped riblets, tip angle $\alpha = 60°$. The statistics errors on the measurements are again omitted because smaller than the significant digits considered, due to the high averaging time of the statistics.

The results for the corner correction case are successfully in agreement with the experimental data also for the lowest resolution case, while the original one has both solutions in the region of drag increase.

Case	Re_τ	Re_b	U_b^+	C_f	$\mathscr{R}$	ΔU^+
EC8	200	3275	16.38	0.00746	+0.039	-0.325
EC16	200	3289	16.44	0.00740	+0.047	-0.392
OC8	200	3037	15.19	0.00867	-0.117	+0.865
OC16	200	3182	15.91	0.00790	-0.018	+0.141

Table 4.2. Turbulent straight riblets results. Re_τ viscous Reynolds number. Re_b bulk Reynolds number. U_b^+ bulk velocity in viscous units. C_f friction coefficient. $\mathscr{R}$ drag reduction. ΔU^+ roughness function.

The streamwise mean velocity profiles in viscous units $\langle u \rangle^+$, and the variances, are also plotted in the wall-normal direction z^+, shifted concerning the normalized longitudinal protrusion height $h_{\parallel}$, Fig.4.2.

(a) (b)
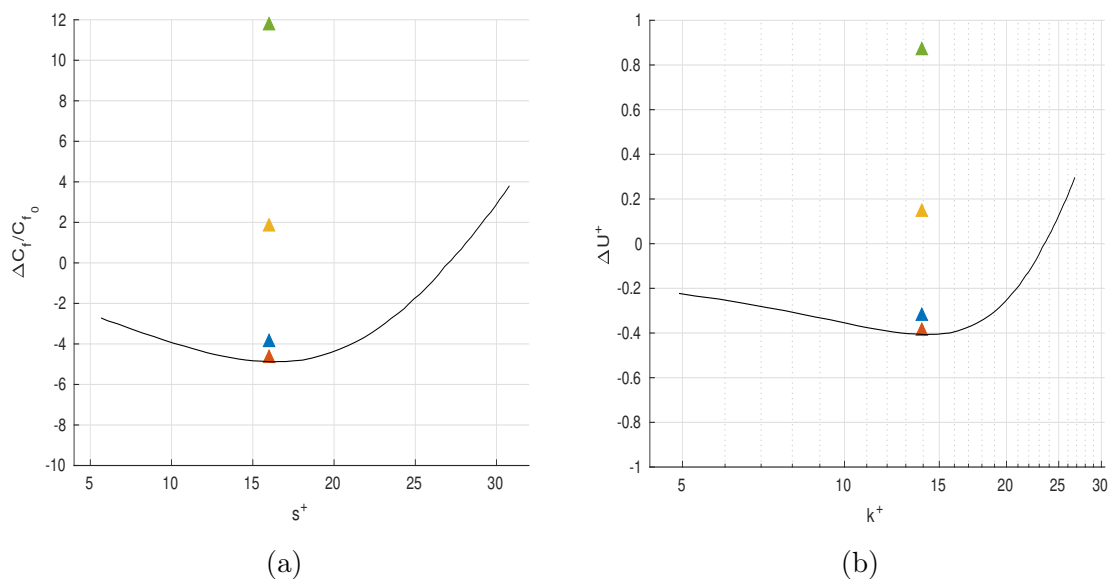
Figure 4.1. Drag reduction curve, $\frac{\Delta C_f}{C_{f_0}} = -\mathscr{R}$ (a) and roughness function curve ΔU^+ (b) as a function of the riblet spacing and the riblet height respectively.

▲ OC8, ▲ OC16, original code case. ▲ EC8, ▲ EC16, edge correction case.
(——) Bechert *et al.* [3] reference data for V-shaped riblets $\alpha = 60°$.

(a) (b)
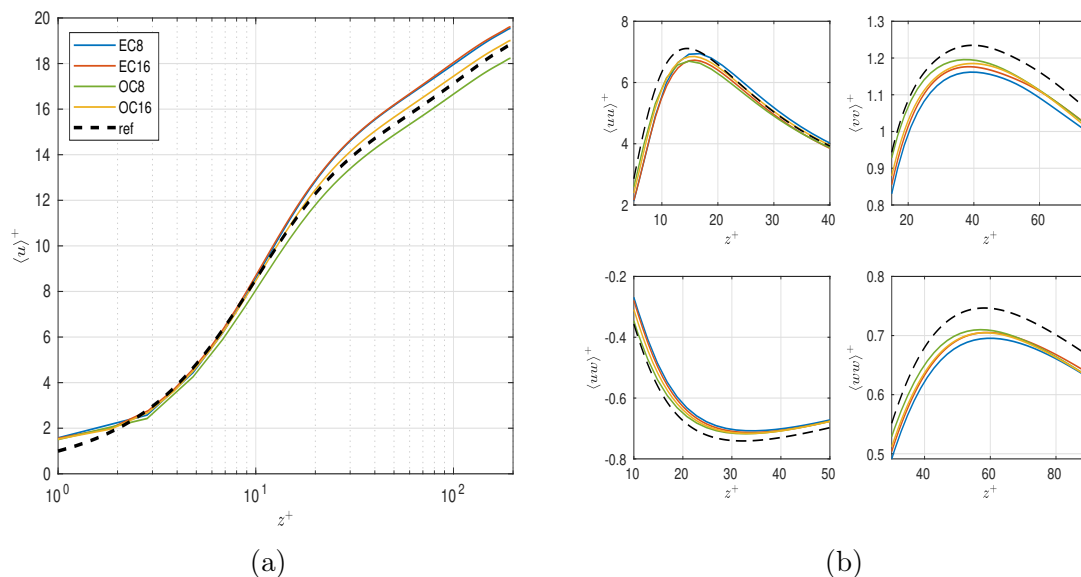
Figure 4.2. Mean streamwise velocity (a) and mean variances (b).
(——) EC8, (——) EC16, edge correction case. (——) OC8, (——) OC16, original code case. (- - - -) reference smooth channel.

4.2   A preliminary experiment on 3D riblets

Once the great potential of the corner correction method is known, it is important to think about the first development of the method itself.

The two-dimensional correction thus implemented is not able to solve the totality of the geometries. It is limited to the capability of studying only edges in the plane of the duct section, therefore for three-dimensional geometries resulting from an extrusion of the section in the streamwise direction.

The objective of the present part is to show a possible generalization of the correction which would also allow to include the possible different orientation of the edge section along x.

The V-shaped riblets of the description made in the first part are again considered, but with a sinusoidal trend in the streamwise direction.

Initially, it is fundamental to understand what is really changing in the problem, compared to the simple case analyzed before. Looking at the problem from afar, it consisted in computing the corner correction for any geometry contained in the plane of the duct section (therefore with direction $\bar{e}_x = [1, 0, 0]$) moving with constant direction and aligned to the streamwise dimension: $\bar{e}_{edge} \equiv \bar{e}_x \quad \forall x$.

On the contrary, the plane containing the section of the immersed body must be able now to shift along x. More precisely the plane is left to freely rotate around the z wall-normal axis, or from the point of view of the directional versor identifying the plane, to change direction in the plane $x - y$. For the example case considered, the problem is shown in Fig.4.3.

Therefore, for a generic point P in the computational domain, the closest edge will be identified by the plane of the edge section that contains that point. The velocity and pressure Stokes solution in the plane will have the same form as the simplest case, and they are recalled below:

$$
\begin{cases}
\tilde{u} = Cr^m \cos{(m\theta)}, \qquad m = \frac{\pi}{2\varphi_{wall}} \\
\tilde{v} = v_r \sin{(\theta)} + v_\theta \cos{(\theta)} \\
\tilde{w} = v_r \cos{(\theta)} - v_\theta \sin{(\theta)} \\
\frac{1}{\nu}p = -4D_3\gamma r^{\gamma-1} \sin{[(\gamma - 1)\theta]}.
\end{cases}
\tag{4.2}
$$

In this way, the polar coordinates of the point P with respect to the corner will be known and so the Stokes solution.

The last step is to project the corner correction in the channel reference system and write the velocity components (u, v, w) through the plane directional versors of the
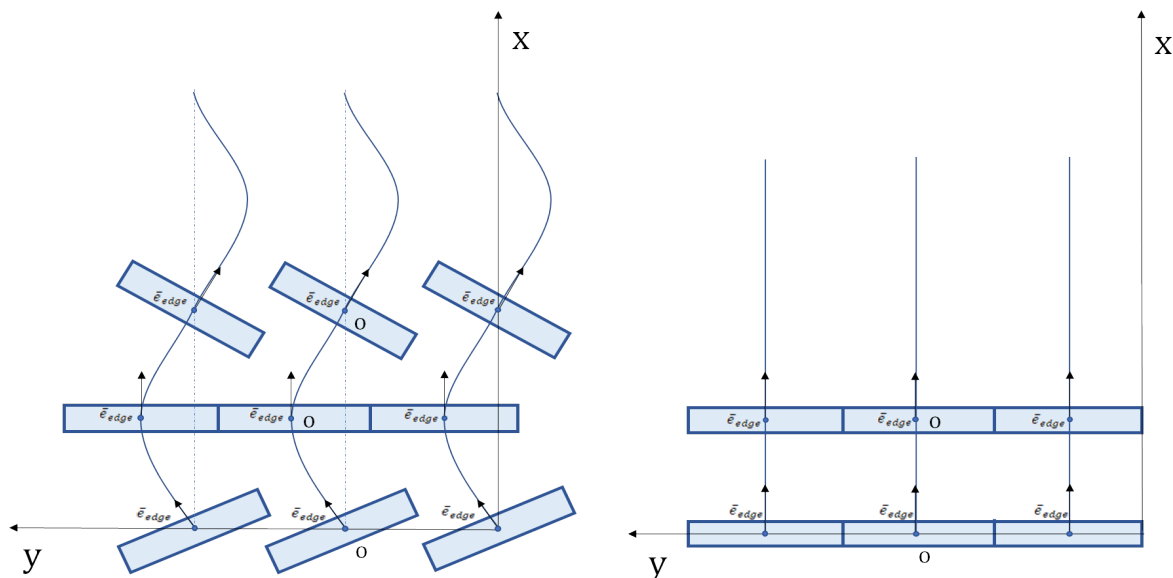
Figure 4.3. Directional versor $\bar{e}_{edge}$ of the plane containing the riblet 2D-section along the streamwise axis for the sinusoidal case (left) and straight case (right).

immersed body section as follows:

$$
\begin{cases}
u = \bar{e}_{edge_x} \cdot \tilde{u} + \bar{e}_{edge_x} \cdot \tilde{v} = \tilde{u} \cos\left(\alpha\right) - \tilde{v} \sin\left(\alpha\right) \\
v = \bar{e}_{edge_y} \cdot \tilde{u} + \bar{e}_{edge_y} \cdot \tilde{v} = \tilde{v} \cos\left(\alpha\right) + \tilde{u} \sin\left(\alpha\right) \\
w = \tilde{w} = v_r \cos\left(\theta\right) - v_\theta \sin\left(\theta\right)
\end{cases}
\tag{4.3}
$$

where α is the rotation angle of the immersed body section plane around the z axis, positive anti-clockwise.

4.3   Results

Three different case studies of sinusoidal riblets are presented. The geometries are defined by two parameters: the wavelength in viscous units λ^+, and the maximum angle of the sine wave α. These two quantities are combined to describe the sinusoid as follows:

$$
\begin{cases}
\lambda = \lambda^+ \cdot Re_\tau \\
A = \tan\left(\alpha \frac{\pi}{180}\right) / \left(\frac{2\pi}{\lambda}\right) \\
y(x) = A \cdot \sin\left(x \frac{2\pi}{\lambda}\right)
\end{cases}
\tag{4.4}
$$

In particular, the first sinusoid is long and not very wide, with $\alpha = 2°$ and $\lambda^+ = 1500$ (standard, STD). Conversely, the second one is shorter $\lambda^+ = 250$ and angled $\alpha = 15°$ (short, SHR). Finally, the third one is given by the superposition of two sinusoids, one
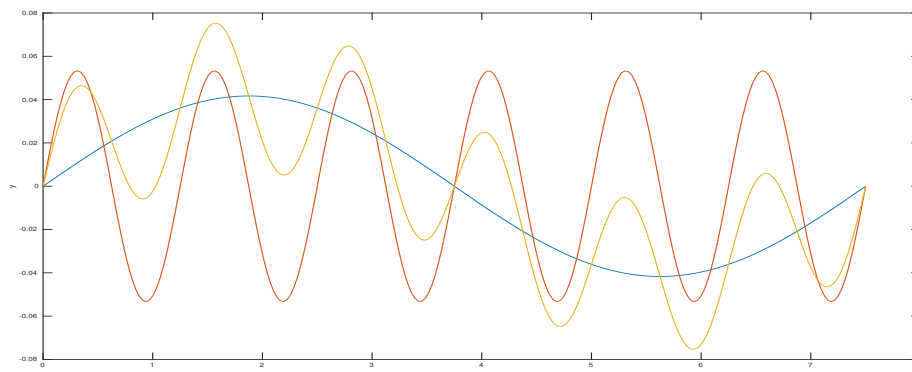
29

Figure 4.4. Riblets sinusoidal trend. (——) STD case, (——) SHR case and (——) CMB
case.

is identical to the first case while the other one is similar to the short case since it
differs for the maximum angle which is $\alpha = 10°$ (combination, CMB).

The simulations are performed for a half-channel, forcing strategy CPG and viscous

Case	Δx^+	Δy^+	$\Delta z^+_{\min}$	$\Delta z^+_{\max}$	h/s	s^+	$A_g^{+1/2}$	α	λ^+
STD	6.6	1.0	1.0	3.0	0.87	16	10.6	2°	1500
SHR	6.3	1.0	1.0	3.0	0.87	16	10.6	15°	250
CMB	6.3	1.0	1.0	3.0	0.87	16	10.6	[2°, 10°]	[250, 1500]

Table 4.3. Simulation parameters. $\Delta^+_{(\cdot)}$ spatial resolutions. $L^+_{(\cdot)}$ domain lengths. h/s riblet
height to spacing ratio. s^+ riblet spacing. $A_g^{+1/2}$ root square of the groove
cross-section. α sinusoid maximum angle. λ^+ wave length. $(\cdot)^+$ viscous units.

Reynolds number $Re_\tau = 200$. The domain sizes are analogous to the straight riblets
($L_x^+ = 1500$ e $L_y^+ = 416$) and the height is $\delta = 1 + h/2$. The number of points in
the spanwise direction is the same for all simulations and equal to the maximum
resolution of the straight riblets: $N_y = 416$, i.e. 16 points per riblet. In the streamwise
direction the STD has $N_x = 226$, while SHR and CMB both have $N_x = 240$. The
computational cells have $A\!\!R = 1$, and the resolutions are reported in Tab.4.3.
The riblets have a ratio $h/s = 0.87$ and a spacing in viscous units $s^+ = 16$, like
the previous cases. The results are therefore presented in Tab.4.4, in terms of drag
reduction and roughness function with respect to the reference plane case.
The spanwise velocity isolines for a portion of the domain section located at a height
that cuts the riblets, are presented in Fig.4.5. The sinusoidal trending of the velocity
is clearly visible.

Case	Re_τ	Re_b	U_b^+	C_f	$\mathscr{R}$	ΔU^+
STD	200	3277	16.39	0.00745	+0.0354	-0.292
SHR	200	3301	16.51	0.00734	+0.0493	-0.411
CMB	200	3277	16.39	0.00745	+0.0355	-0.293

Table 4.4. Turbulent sinusoidal riblets results. Re_τ viscous Reynolds number. Re_b bulk Reynolds number. U_b^+ bulk velocity in viscous units. C_f friction coefficient. $\mathscr{R}$ drag reduction. ΔU^+ roughness function.
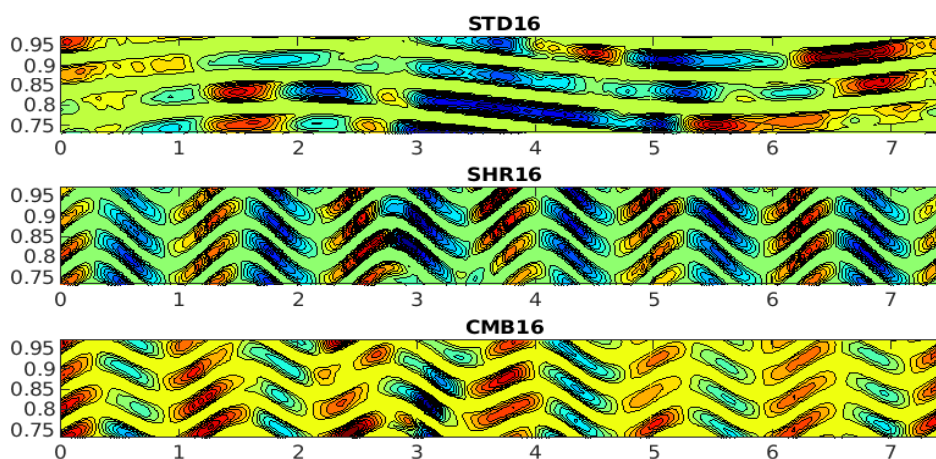

Figure 4.5. Spanwise velocity isolines on a plane portion located at $z = 0.01$ for the STD, SHR and CMB cases.

Conclusions

In the present study, a corner correction method has been presented both from the analytical and implementational point of view. Firstly, it was validated by the computation of the normalized protrusion heights in simple Stokes flow, for a V-shaped riblet, tip angle $\alpha = 60°$ and $h/s = 0.87$, compared with the analytical data of Luchini [17]. It was possible to quantify the computational efficiency improvement approximately by an order of magnitude, according to the difference of the points per riblet used between the corrected code and the original one to obtain the same error on Δh.

The final verification was then carried out in a turbulent half-channel flow at a viscous Reynolds number $Re_\tau = 200$, with CPG forcing strategy, in correctly measuring the drag reduction for two resolution cases: 8 and 16 points per riblet. The simulation was performed around the optimum of the drag reduction curve, more precisely for $s^+ = 16$.

Matching the results obtained in terms of drag reduction $\mathscr{R}$ and roughness function ΔU^+ with the Bechert *et al.* [3] data, Tab.4.2 and Fig.4.1, the definitive confirmation of the potential of the corner correction method was achieved. In fact the original code was unable, even in the higher resolution case, to measure positive drag reduction $\mathscr{R}\% = -1.8\%$. While the code with edge correction, measured the drag reduction in both resolution cases, and in the high resolution one the value is within the 2% error with respect to the Bechert *et al.* [3] interpolated data: $\mathscr{R}\% = +4.7\%$.

Later an extension of the corner correction method was shown in order to include also those geometries in which the directional versor identifying the plane containing the body section can freely rotate around the wall-normal axis z along the streamwise direction x. Three different configurations of sinusoidal riblets (STD: $\alpha = 2°$, $\lambda^+ = 1500$; SHR: $\alpha = 15°$, $\lambda^+ = 250$; CMB: $\alpha = [2°, 10°]$, $\lambda^+ = [1500, 250]$) in turbulent half-channel flow at $Re_\tau = 200$ and CPG have been considered. The section of the riblet was identical to the previous case: V-shaped, tip angle $\alpha = 60°$ and $s^+ = 16$. The resolution adopted was 16 points per riblet for all three cases, and the results

were presented in Tab.4.4 in terms of drag reduction and roughness function. For each case the drag reduction was obtained, and only the SHR improved the drag reduction compared to straight riblets.

Appendix A

The parts of the code described in § 3.2 are here reported.

Listing 1. Real function *edge*

```
105  STRUCTURED ARRAY(y,z) OF REAL FUNCTION edge(REAL yp,zp)
106  ! (yp,zp) point coordinates --> coordinates edge nearest
107    RESULT.y=[FLOOR(yp/spacing)+0.5]*spacing
108    RESULT.z=0.5*height
109  END edge
```

Listing 2. function *locsol* in the subroutine of the immersed boundary correction

```
118  REAL phiwall=PI-phirib
119  BOOLEAN FUNCTION stokdisp(REAL stokexp)=SIN(2*stokexp*phiwall)
120      +stokexp*SIN(2*phiwall)>0
121  stokexp=Bisection(stokdisp,0.5120772,0.5120774)  ! constant gamma
122  C1=1 ! D1
123  C2=-COS((stokexp+1)*phiwall)/COS((stokexp-1)*phiwall)*C1 ! D3
124  Clap=1  ! 1 for ulap correction on
125  REAL lapexp=PI/(2*phiwall) ! m constant of the laplace solution
126  REAL theta=0,rho=0
127  REAL FUNCTION locsol(REAL yp,zp)
128      IF InBody(1*deltax,yp,zp) THEN RETURN 0
129      !compute theta e r
130      theta=atan2(yp-edge(yp,zp).y, zp-edge(yp,zp).z)
131      rho=SQRT[(yp-edge(yp,zp).y)^2+(zp-edge(yp,zp).z)^2]
132      !Compute vr and vt according to Stokes solution
133      vr=rho^(stokexp)*[-C1*(stokexp+1)*SIN((stokexp+1)*theta)-
134                        C2*(stokexp-1)*SIN((stokexp-1)*theta)]
135      vt=-(stokexp+1)*rho^(stokexp)*[C1*COS((stokexp+1)*theta)+
136                                     C2*COS((stokexp-1)*theta)]
137      !u according to Laplace solution
```

```
138    ulap=Clap*rho^(lapexp)*COS(lapexp*theta)
139    ! return u_st, v_st, w_st depending on the direction considered
140    IF dix#0 THEN RESULT=ulap
141    IF diy#0 THEN RESULT=vr*SIN(theta)+vt*COS(theta)
142    IF diz#0 THEN RESULT=vr*COS(theta)-vt*SIN(theta)
143 END locsol
```

Listing 3. Function *lopsol* in the subroutine of the immersed boundary correction

```
144 REAL FUNCTION locpsol(REAL yp,zp)
145    theta=atan2(yp-edge(yp,zp).y, zp-edge(yp,zp).z)
146    rho=SQRT[(yp-edge(yp,zp).y)^2+(zp-edge(yp,zp).z)^2]
147    IF rho=0 THEN RETURN 0
148    !smoothing the pressure singularity at vr=0
149    ARRAY[0..nz-1] OF REAL deltaz
150    DO deltaz(izz)=zd(izz+1)-zd(izz) FOR izz=0 TO nz-1
151    REAL ddeltaz=MIN(deltaz)
152    !for rho->0 rho^(stokexp-1)-> Inf, smoothing correction
153    IF rho<ddeltaz THEN rho=rho*(ddeltaz)^(stokexp-2)
154    ELSE rho=rho^(stokexp-1)
155    !p continuous and symmetric inside the solid wall
156    IF ABS(theta)>phiwall THEN
157       theta=theta*[1+(ABS(theta)-phiwall)/(PI-phiwall)*
158                                  [1/(stokexp-1)-1]]
159    !p_st(rho,theta)/nu
160    RESULT=-4*C2*stokexp*rho*SIN((stokexp-1)*theta)
161 END locpsol
```

Listing 4. Composition of the edge correction coefficient in the subroutine of the immersed boundary correction

```
178 IF InBody(x,y,z) THEN rsd=1E20 ELSE
179    !if the point is near to the edge (corrthck=3)
180    IF (y-edge(y,z).y)^2+(z-edge(y,z).z)^2<=(corrthck*deltay)^2
181    THEN
182       weight=locsol(y,z)
183       IF weight=0 THEN
184          rsd=1E20
185       ELSE
186       !1/nu*[1/u_st*(p_st((ix-dix)*dx)-p_st((ix+dix)*dx))]/dx
```

```
187            weight =1/ weight
188            rsd =~+ weight *( locpsol [iy* deltay ,zd (2* iz )]
189                 - locpsol [( iy+diy )* deltay ,zd (2*( iz+diz ))])/
190                 ( deltax *dix+ deltay *diy+zd [2*( iz+diz )] -zd [2* iz ])
191          END IF
192       END IF
193    REAL d= deltax
194    IF InBody [x- deltax ,y,z]
195    THEN d=x- Bisection [ InBody (* ,y,z),x- deltax ,x]
196          IF d=0 THEN rsd =1E20
197          ELSE
198          !1/ dx/dx * dx/ d_x2 *u_st (x- d_x2 )/ u_st (x)
199             IF [(y- edge (y,z).y )^2+(z- edge (y,z).z )^2 <=
200                                 ( corrthck * deltay )^2]
201             THEN rsd =~+ limited [ locsol (y,z)* weight ]* deltax /d* d2x
202             ELSE rsd =~+ deltax /d* d2x
203       END IF
204       d= deltax
205    IF InBody (x+ deltax ,y,z)
206    THEN d= Bisection [ InBody (* ,y,z),x,x+ deltax ]-x
207          IF d=0 THEN rsd =1E20
208          ELSE
209          !1/ dx/dx * dx/ d_x1 * u_st (x+ d_x1 )/ u_st (x)
210             IF [(y- edge (y,z).y )^2+(z- edge (y,z).z )^2 <=
211                                 ( corrthck * deltay )^2]
212             THEN rsd =~+ limited [ locsol (y,z)* weight ]* deltax /d* d2x
213             ELSE rsd =~+ deltax /d* d2x
214       END IF
215       d= deltay
216    IF InBody (x,y- deltay ,z)
217    THEN d=y- Bisection [ InBody (x,* ,z),y- deltay ,y]
218          IF d=0 THEN rsd =1E20 ELSE
219          !1/ dy/dy * dy/ d_y2 * u_st (y- d_y2 )/ u_st (y)
220             IF [(y- edge (y,z).y )^2+(z- edge (y,z).z )^2 <=
221                                 ( corrthck * deltay )^2]
222             THEN rsd =~+ limited [ locsol (y-d,z)* weight ]* deltay /d* d2y
223             ELSE rsd =~+ deltay /d* d2y
224       END IF
```

```
225     d=deltay
226   IF InBody(x,y+deltay,z)
227   THEN d=Bisection[InBody(x,*,z),y,y+deltay]-y
228         IF d=0 THEN rsd=1E20 ELSE
229         !1/dy/dy * dy/d_y1 * u_st(y+d_y1)/u_st(y)
230           IF [(y-edge(y,z).y)^2+(z-edge(y,z).z)^2<=
231                                         (corrthck*deltay)^2]
232           THEN rsd=~+limited[locsol(y+d,z)*weight]*deltay/d*d2y
233           ELSE rsd=~+deltay/d*d2y
234     END IF
235     ! deltazm and deltazp because of non-uniform grid
236     d=deltazm
237   IF InBody(x,y,z-deltazm)
238   THEN d=z-Bisection[InBody(x,y,*),z-deltazm,z]
239         IF d=0 THEN rsd=1E20 ELSE
240         !1/dz/dz * dz/d_z2 * u_st(z-d_z2)/u_st(z)
241           IF [(y-edge(y,z).y)^2+(z-edge(y,z).z)^2<=
242                                         (corrthck*deltay)^2]
243           THEN rsd=~+limited[locsol(y,z-d)*weight]*deltazm/d*d2zm
244           ELSE rsd=~+deltazm/d*d2zm
245     END IF
246     d=deltazp
247   IF InBody(x,y,z+deltazp)
248   THEN d=Bisection[InBody(x,y,*),z,z+deltazp]-z
249         IF d=0 THEN rsd=1E20 ELSE
250         !1/dz/dz * dz/d_z1 * u_st(z+d_z1)/u_st(z)
251           IF [(y-edge(y,z).y)^2+(z-edge(y,z).z)^2<=
252                                         (corrthck*deltay)^2]
253           THEN rsd=~+limited[locsol(y,z+d)*weight]*deltazp/d*d2zp
254           ELSE rsd=~+deltazp/d*d2zp
255     END IF
256 END IF
257 ! .. - 2/dx/dx - 2/dy/dy - 2/dz/dz
258 imbc(ix,iy,iz)=[rsd-2*d2x-2*d2y-d2zm-d2zp]*nu
```

Appendix B

Streamwise velocity isolines u of the instantaneous field for the different cases described in the § 4 of V-shaped straight riblets are here shown for a portion of the domain. It can be easily noticed that the fields resulting from the code with edge correction (EC) have a higher speed in the centreline than the cases resulting from the original code (OC).
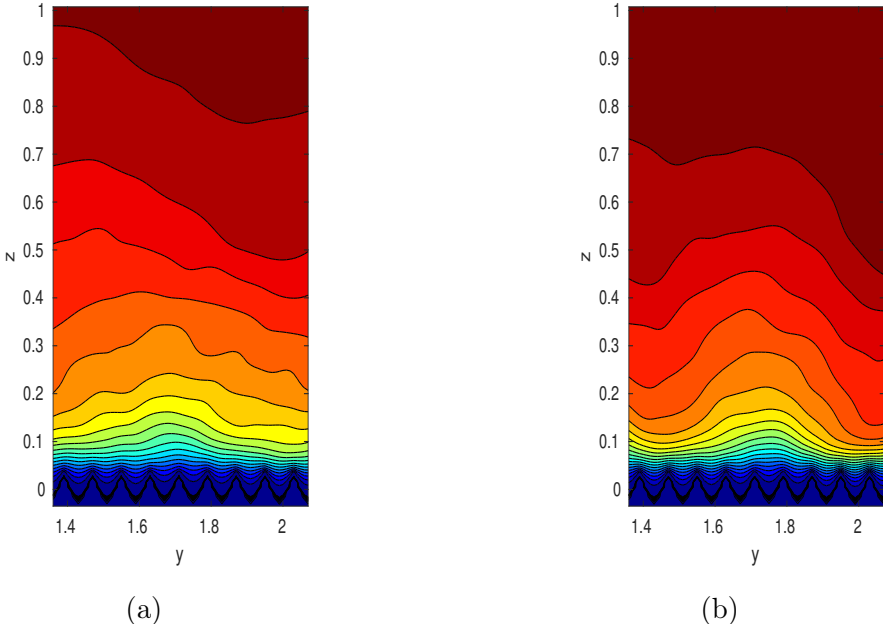
(a)

(b)

Figure B.1. Streamwise velocity isolines for a portion of an instantaneous velocity field. (a) original case, 8 points per riblet. (b) corner correction case, 8 points per riblet.
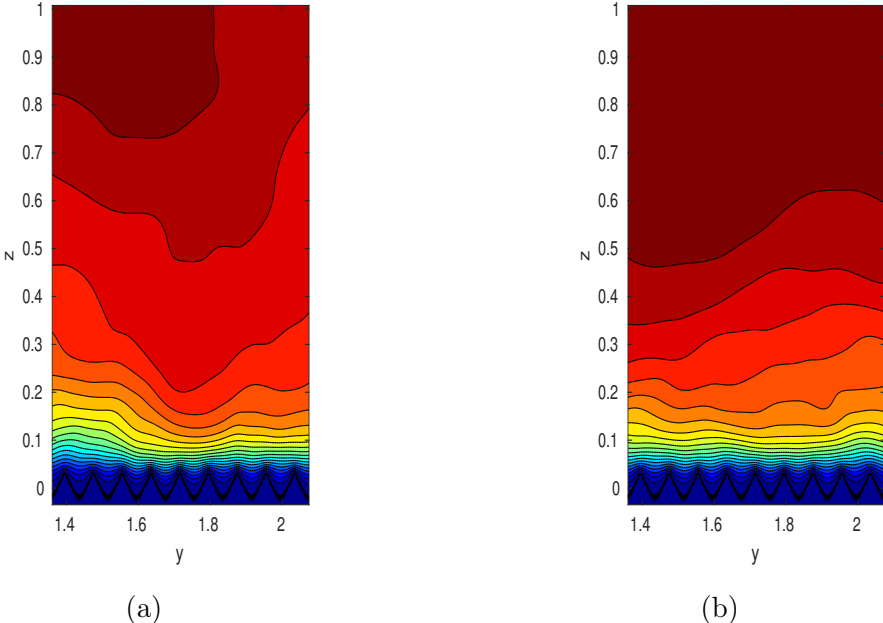

(a)

(b)

Figure B.2. Streamwise velocity isolines for a portion of an instantaneous velocity field. (a) original case, 16 points per riblet. (b) corner correction case, 16 points per riblet.

Bibliography

[1] BANCHETTI, J., LUCHINI, P., AND QUADRIO, M. Turbulent drag reduction over curved walls. *Journal of Fluid Mechanics 896* (Aug. 2020). Publisher: Cambridge University Press.

[2] BECHERT, D., AND REIF, W. On the Drag Reduction of the Shark Skin. In *23rd Aerospace Sciences Meeting*. American Institute of Aeronautics and Astronautics, 1985.

[3] BECHERT, D. W., BRUSE, M., HAGE, W., HOEVEN, J. G. T. V. D., AND HOPPE, G. Experiments on drag-reducing surfaces and their optimization with an adjustable geometry. *Journal of Fluid Mechanics 338* (May 1997), 59–87. Publisher: Cambridge University Press.

[4] BROWN, G. L., AND ROSHKO, A. On density effects and large structure in turbulent mixing layers. *Journal of Fluid Mechanics 64*, 4 (July 1974), 775–816.

[5] BRUSE, M., BECHERT, D. W., VAN DER HOEVEN, J. G. T., HAGE, W., AND HOPPE, G. Experiments with Conventional and with Novel Adjustable Drag-reducing Surfaces. In *International Conference on Near-Wall Turbulent Flows.* (Tempe, Arizona, USA, Mar. 1993).

[6] BURDAK, V. Function of the ctenoid apparatus of fish in the presence of a turbulent boundary layer. *Zool. Zh.*, 48 (1969), 1053–1055.

[7] CHERNYSHOV, O., AND ZAYETES, V. Some peculiarities of the structure of the skin of sharks. *Hydrodynamic Problems of Bionics Bionica*, Nr.4 (1970), 77–83.

[8] CHOI, K. S. Test of Drag Reducing Riblets on a One-third Scale Racing Yacht. *Turbulent Drag Reduction by Passive Means, Royal Aero. Soc. London* (1987), 377–391.

[9] ENDRIKAT, S. *Effects of riblet shape on drag reduction in turbulent flow.* PhD thesis, University of Melbourne, 2020.

[10] García-Mayoral, R., and Jiménez, J. Drag reduction by riblets. *Philosophical Transactions of the Royal Society A: Mathematical, Physical and Engineering Sciences 369*, 1940 (Apr. 2011), 1412–1427.

[11] García-Mayoral, R., and Jiménez, J. Hydrodynamic stability and breakdown of the viscous regime over riblets. *Journal of Fluid Mechanics 678* (July 2011), 317–347.

[12] Gatti, D., Cimarelli, A., Hasegawa, Y., Frohnapfel, B., and Quadrio, M. Global energy fluxes in fully-developed turbulent channels with flow control. *Journal of Fluid Mechanics 857* (Dec. 2018), 345–373.

[13] Gatti, D., von Deyn, L., Forooghi, P., and Frohnapfel, B. Do riblets exhibit fully rough behaviour? *Experiments in Fluids 61*, 3 (Mar. 2020), 81.

[14] Kline, S. J., Reynolds, W. C., Schraub, F. A., and Runstadler, P. W. The structure of turbulent boundary layers. *Journal of Fluid Mechanics 30*, 4 (Dec. 1967), 741–773.

[15] Luchini, P. Higher-order difference approximations of the Navier-Stokes equations. *International Journal for Numerical Methods in Fluids 12*, 5 (Mar. 1991), 491–506.

[16] Luchini, P. Immersed-boundary simulation of turbulent flow past a sinusoidally undulated river bottom. *European Journal of Mechanics - B/Fluids 55* (2016), 340–347.

[17] Luchini, P., Manzo, F., and Pozzi, A. Resistance of a grooved surface to parallel flow and cross-flow. *Journal of Fluid Mechanics Digital Archive 228* (July 1991), 87.

[18] McLean, J., George-Falvy, D., and Sullivan, P. Flight-test of turbulent skin- friction reduction by riblets. *Proc. Turbulent Drag Reduction by PassiveMeans R. Aero. Soc.* (Sept. 1987).

[19] Robert, J. P. Drag Reduction: An Industrial Challenge. Tech. rep., AIRBUS INDUSTRIE BLAGNAC (FRANCE), Mar. 1992. Section: Technical Reports.

[20] Sawyer, W. G., and Winter, K. G. An investigation of the effect on turbulent skin friction of surfaces with streamwise grooves. *Turbulent Drag Reduction by*

Passive Means 2 (Jan. 1987), 330A–362. Conference Name: Turbulent Drag Reduction by Passive Means.

[21] SPALART, P. R., AND MCLEAN, J. D. Drag reduction: enticing turbulence, and then an industry. *Philosophical Transactions of the Royal Society A: Mathematical, Physical and Engineering Sciences 369*, 1940 (Apr. 2011), 1556–1569. Publisher: Royal Society.

[22] SZODRUCH, J. Viscous drag reduction on transport aircraft. In *29th Aerospace Sciences Meeting*, Aerospace Sciences Meetings. American Institute of Aeronautics and Astronautics, Jan. 1991.

[23] WALSH, M., AND LINDEMANN, A. Optimization and application of riblets for turbulent drag reduction. In *22nd Aerospace Sciences Meeting*. American Institute of Aeronautics and Astronautics, 1984.

[24] WALSH, M. J. Effect of detailed surface geometry on riblet drag reduction performance. *Journal of Aircraft 27*, 6 (June 1990), 572–573.

[25] WALSH, M. J., III, W. L. S., AND MCGINLEY, C. B. Riblet drag at flight conditions. *Journal of Aircraft* (May 2012).